

For Reference

NOT TO BE TAKEN FROM THIS ROOM

Ex LIBRIS
UNIVERSITATIS
ALBERTAEASIS



THE UNIVERSITY OF ALBERTA

ANALYSIS OF MAGNETIC AMPLIFIER CIRCUITS THROUGH
MODELING OF IRON-CORE TRANSFORMERS

by



ZEINAB M. YOUSSEF (nee EL-GAZAERLY)

A THESIS

SUBMITTED TO THE FACULTY OF GRADUATE STUDIES
IN PARTIAL FULFILMENT OF THE REQUIREMENTS FOR THE DEGREE
OF MASTER OF SCIENCE.

DEPARTMENT OF ELECTRICAL ENGINEERING

EDMONTON, ALBERTA

FALL, 1971

ABSTRACT

A mathematical model to represent hysteresis in dynamic systems was proposed in a recent paper by Chua and Stromsmoe [8]. In the case of iron-core inductors and transformers the model has an extremely simple circuit interpretation, namely a parallel combination of a nonlinear resistor and nonlinear inductor and ideal transformers. In the previous work several experimental results were compared to those predicted by the model. All examples were limited to circuits containing either an iron-core inductor or an iron-core transformer.

In the present work the same model is used to examine circuits containing two iron-core transformers. The specific circuits considered are the parallel and series connected non-feedback magnetic amplifiers. In both circuits the magnetizing current is appreciable in comparison to the total current. Thus the model must accurately account for both large nonlinear effects and appreciable hysteretic losses.

The magnetic amplifier is operated under a wide range of conditions, the simulated and measured results are compared. The close agreement between these indicate that the model is remarkably good in predicting the performance of the magnetic amplifier.

ACKNOWLEDGMENTS

The author wishes to express her gratitude and indebtedness to Dr. K.A. Stromsmoe, under whose supervision this work was carried out, for his invaluable suggestions and constructive criticism throughout the course of this work.

Special thanks must go to Dr. G.B. Walker for his support during the course of studies.

The author would like to acknowledge the financial support of the National Research Council.

The work described in this thesis was carried out at the Department of Electrical Engineering, University of Alberta.

Digitized by the Internet Archive
in 2023 with funding from
University of Alberta Library

TABLE OF CONTENTS

	Page
Chapter 1	1
1.1 Introduction	1
1.2 Objective of this study	3
1.3 Magnetic amplifiers	4
Chapter 2 THE MATHEMATICAL MODEL	8
2.1 Mathematical representation	8
2.2 Iron-core transformer	9
2.3 Determination of $f(\cdot)$ and $g(\cdot)$	12
2.4 Model for the magnetic amplifier cores	17
Chapter 3 PARALLEL-CONNECTED MAGNETIC AMPLIFIER	22
3.1 Theory of operation	22
3.2 Analysis	25
3.3 Numerical computation	38
3.4 Experimental results	43
3.5 Comparison	44
Chapter 4 SERIES-CONNECTED MAGNETIC AMPLIFIER	54
4.1 Theory of operation	54
4.2 Analysis	55
4.3 Numerical computation	64
4.4 Experimental results	65
4.5 Comparison	65

	Page
Chapter 5	CONCLUSION
	73
REFERENCES	75
APPENDIX A	THE PIECEWISE LINEARIZATION TECHNIQUE
	77
APPENDIX B	FLOW-CHARTS
	79

LIST OF FIGURES

		Page
Figure 2.1	Lumped Circuit model for an iron-core inductor	11
2.2	Lumped Circuit model for an iron-core transformer	11
2.3	Construction procedure for determining the restoring function $f(\cdot)$ and the dissipation function $g(\cdot)$	16
2.4	Lumped Circuit model for two cores with common control winding	18
2.5	Hysteresis loop computed using the lumped circuit model	21
2.6	Experimental hysteresis loop	21
3.1	Parallel-connected magnetic amplifier	23
3.2	The equivalent circuit of parallel-connected magnetic amplifier using the nonlinear lumped circuit model	26
3.3	The equivalent circuit for the parallel-connected magnetic amplifier after referring all the circuit elements to the load side	27

		Page
Figure 3.4	The final equivalent circuit of the parallel-connected magnetic amplifier	28
3.5	The $i-\lambda$ curve (a) for the nonlinear inductors and $v-i$ curve (b) for the nonlinear resistors	41
3.6	Experimental and computed voltage waveforms for $E_C = 0.0$	47
3.7	Experimental and computed voltage waveforms for $E_C = 5$	48
3.8	Experimental and computed voltage waveforms for $E_C = 10$	49
3.9	Experimental and computed voltage waveforms for $E_C = 15$	50
3.10	Experimental and computed voltage waveforms for $E_C = 20$	51
3.11	Experimental and computed voltage waveforms for $E_C = 25$	52
3.12	Experimental and computed voltage waveforms for $E_C = 30$	53
4.1	Series-connected magnetic amplifier	56
4.2	The equivalent circuit for the series-connected magnetic amplifier using the nonlinear lumped circuit model	58

		Page
Figure 4.3	Circuit diagram for the series-connected magnetic amplifier replacing ideal transformers by equivalent controlled source representation	59
4.4	Experimental and computed voltage waveforms for $E_C = 0.0$	68
4.5	Experimental and computed voltage waveforms for $E_C = 10$	69
4.6	Experimental and computed voltage waveforms for $E_C = 20$	70
4.7	Experimental and computed voltage waveforms for $E_C = 30$	71
4.8	Experimental and computed voltage waveforms for $E_C = 40$	72
A.1	The parameters defining a piecewise-linear segment	78

CHAPTER 1

1.1 Introduction

Hysteresis is a phenomenon that is observed in many materials and processes. Hysteresis is observed in the flux versus magnetization force relationship of ferromagnetic and ferrimagnetic materials [1-3], in dielectrics [4], and in the stress-strain relationship of materials that undergo plastic deformation. The human respiratory system is another example of a process where hysteresis occurs [5]. In order to analyze systems, in particular circuits, containing hysteretic elements, it is necessary to have a mathematical model which can replace the hysteretic elements and closely simulates the hysteresis phenomenon.

To solve this modeling problem several mathematical models have been reported. These mainly follow two basic approaches, the first approach [6] is a physical one based on the physical principles governing the behavior of the hysteretic elements, and the second approach [7] is based on postulating a suitable mathematical representation which can be shown to exhibit hysteresis phenomenon. The first approach results in mathematical models in the form of partial differential equations, and even with the help of a computer the analysis of nonlinear systems or circuits containing the hysteretic elements described by these differential equations will be difficult.

The second approach results in nonlinear mathematical models.

The model used in the present work is based on this approach [8]. The establishment of the accuracy and validity of these models in simulating hysteretic elements is not an easy process. For linear models there is a valid representation theorem [9] stating that if a linear model is found to give an exact response, such as impulse response, corresponding to a given test signal, then the model will give the correct response to all other test signals. This representation theorem is not valid for nonlinear models since its proof makes use of the principle of superposition. Without a representation theorem, analogous to that of linear systems, it is difficult to establish the validity of nonlinear models. This is the main difficulty inherent in the second approach where the establishment of the validity of the nonlinear model requires an infinite set of measurements corresponding to all possible excitation signals.

Actually the validity of any of the models based on this second approach is first established qualitatively by showing that the postulated model exhibits the same significant properties and features of the hysteretic elements, such as expansion of the loop with increase in frequency and the presence of minor loops. The second step is to construct the functions and parameters of the mathematical representation so that the resulting model would yield realistic response to one or more test signals. The model is then assumed to yield reasonably accurate responses to other excitations.

The exactness of the model in representing the hysteretic elements depends on its accuracy in predicting the correct solutions when imbedded in a large number of systems under a variety of excitations. Therefore the ultimate verdict on the usefulness of the model will not be known until sufficient data is gathered concerning its ability to simulate the correct solutions to a large number of practical problems.

1.2 Objective of this study

A mathematical representation based on the second approach was reported recently [8]. This model is a simple one and is very useful for analysis of practical circuits containing hysteretic elements. A major advantage of this mathematical representation is that all its functions can be determined from a given measurement. This mathematical model is an important and useful one especially in the case of iron-core inductors. For such inductors the mathematical representation is found to be equivalent to a simple lumped circuit model. This lumped circuit model makes it possible to analyze circuits containing iron-core inductors or iron-core transformers by simple computer programs.

This mathematical model was proved qualitatively to exhibit most of the significant properties and features of the hysteretic elements. As a step in proving how accurate this model is, it was shown [8] that this model yields realistic results when used to represent the hysteretic elements in a push-pull tunnel diode relaxation

oscillator which use a saturable reactor and tunnel diodes. The model was found to give a very good prediction concerning the frequency, the waveform and amplitude of the generated signal.

As a second step in checking the exactness of this mathematical model, the present work is intended to check its ability and usefulness in analyzing another practical circuit which is the magnetic amplifier. In the case of the push-pull tunnel diode relaxation oscillator there was only one iron-core transformer while in the case of the magnetic amplifier there are two iron-core transformers. The magnetic amplifier is analyzed using the pre-described model to represent the two iron-core transformers. The waveforms and amplitudes of the different voltages in this practical circuit are computed numerically. These are then compared to the actual experimental waveforms and amplitudes of the corresponding voltages, the agreement is found to be excellent.

1.3 Magnetic amplifiers

Magnetic amplifiers are devices which use a small applied input signal to control the voltage or power output. The input signal is at a power level much lower than that of the output power. The magnetic amplifier consists of a combination of saturable reactors, rectifiers, resistors and transformers. The operation of the magnetic amplifier is based on the characteristics of the single saturable reactor. A saturable reactor has a ferromagnetic core and two windings, one of these is the d.c. or control winding N_c and the

other is the a.c or gate winding N_g . For optimum performance of the magnetic amplifier, the core material of its saturable reactors should have the following magnetic properties:-

1. Hysteresis and eddy-current losses a minimum.
2. High saturation flux density, to obtain large power handling capacity of a given weight of core material.
3. The general shape of the hysteresis loop as close as possible to a thin rectangular one.
4. Stability of magnetic characteristics under changing temperature, mechanical strain and shock conditions.

The last property ensures that the characteristics shall not change under varying operating conditions. The first three properties ensure that a small change in the control current (input), flowing through the control winding, varies the magnetization state of the ferromagnetic core over wide limits. This results in a wide range of variation of the inductive impedance of the gate winding. Thus the impedance of the gate winding is dependent on and controlled by the value of the d.c. control current. This principle was used to construct different types of magnetic amplifiers. In all these types the magnitude of the control signal controls the amplitude and the waveform of the voltage across, and hence the power delivered to, the load. This controllability together with the high ratio of the output power to the load to the input power to the control circuit

provide the desired controllable high gain in magnetic amplifiers.

Like other types of amplifiers the gain of the magnetic amplifier increases when positive internal (intrinsic) or external (extrinsic) feedback is introduced. Generally the single-stage and multi-stage magnetic amplifiers used in commercial and industrial applications make use of this positive feedback to allow for higher power amplification [10]. However, it must be noted that the operation of these feedback magnetic amplifiers is based on the characteristics of the non-feedback type. In addition, it must be noted that the presence of the many applications of the feedback magnetic amplifiers does not imply that those without feedback do not serve a useful purpose. Despite the lack of high power gain of the latter, they are relatively simple and have great versatility and do have certain important and useful applications [10-11]. Actually a common factor amongst all types of magnetic amplifiers is that they have extremely high reliability, long life, ruggedness, no warm-up time, high efficiency, a minimum maintainance problem and are capable of high temperature operation.

The present work deals only with the parallel and series connected non-feedback type of magnetic amplifiers. As their names imply, the series-connected type has its gate windings connected in series while the parallel-connected type has its gate windings connected in parallel. The parallel-connected magnetic amplifier has a much slower response to control signals than that of the series-

connected magnetic amplifier [10]. The parallel-connected magnetic amplifier is therefore used in high-power applications where the speed of the amplifier response to changes in control signal is not of prime concern, while the series-connected magnetic amplifier is usually used in applications where nominal power is required and where maximum control speed is required.

CHAPTER 2

THE MATHEMATICAL MODEL

2.1 Mathematical representation

Hysteresis, as stated before, is a phenomenon exhibited by many devices. The present work deals mainly with the hysteresis observed in magnetic materials, for example iron-core inductors or transformers. For magnetic materials the two variables exhibiting the hysteresis phenomenon are the flux linkage $\lambda(t)$ and the winding current $i(t)$ causing this flux linkage to exist. The mathematical model, whose accuracy in representing magnetic materials is to be examined in this work, is a dynamic model. This model relates the two variables $\lambda(t)$ and $i(t)$ through the differential equation,

$$\frac{d\lambda}{dt} = g \circ [i(t) - f(\lambda)] \quad (2.1)$$

This differential equation completely defines this mathematical model. The two functions $f(\cdot)$ and $g(\cdot)$ are real - valued functions defined on the real line R and the symbol "o" denotes the composition operation. The detailed properties of this mathematical model, together with the proofs are in reference [8]. The proving of these properties depends on the fact that the two functions $f(\cdot)$ and $g(\cdot)$ should satisfy the following conditions,

- (i) They are strictly monotonically increasing functions.
- (ii) Both are differentiable onto functions.
- (iii) The two functions have non-zero slopes throughout the entire real line.
- (iv) They should satisfy the property $g(0) = f(0) = 0$.

The function $g(\cdot)$ is called the dissipation function since it can be shown to be responsible for the energy dissipation in the element while $f(\cdot)$ is called the restoring function since it is responsible for the energy storage in the element. This mathematical model can represent any of the hysteretic magnetic materials. In the present work only iron-core transformers are to be replaced by such a model.

2.2 Iron-core transformer

The mathematical model defined by equation (2.1) has many advantages, the most important one is that it yields a lumped circuit model that simulates the hysteretic behavior of an iron-core inductor. This lumped circuit model is shown in Fig. 2.1. Unlike the linear inductors and resistors, it is necessary for nonlinear resistors and inductors to indicate the positive direction of the current flowing through each. Thus each of the two nonlinear elements in Fig. 2.1 is represented by a rectangular symbol having one of its ends darkened. This dark end is the negative end of the nonlinear element and the positive current flows from the positive end to the negative end. Inside the rectangular symbols

the conventional representations of inductors and resistors are used. The lumped circuit shown in Fig. 2.1 consists of a nonlinear inductor "L" in parallel with a nonlinear resistor "R". The nonlinear resistor "R" is defined by the relation between its current i_R and the voltage across its terminals v_R . The characteristic equation of this resistor is,

$$v(t) = v_L = \frac{d\lambda}{dt} = v_R = g(i_R) \quad (2.2)$$

The nonlinear inductor "L" is defined by the relation between its current i_L and the flux λ linking the iron-core inductor. The characteristic equation of this inductor is,

$$i_L = f(\lambda) \quad (2.3)$$

It is clear from this lumped circuit model that the function $g(\cdot)$ is responsible for the energy dissipation in the iron-core inductor, while the function $f(\cdot)$ is responsible for the energy storage. This circuit model of the iron-core inductor is used to obtain the circuit model for an iron-core two winding transformer. Thus the transformer will be completely represented by the circuit model shown in Fig. 2.2. The nonlinear resistor and inductor are defined by the characteristic equations (2.2) and (2.3) respectively, where $v(t)$ is the voltage across one of the two windings of the transformer and

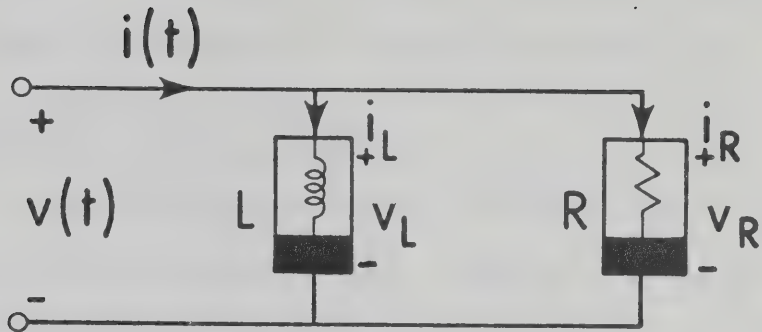


FIG. 2.1

Lumped circuit model for an iron-core inductor

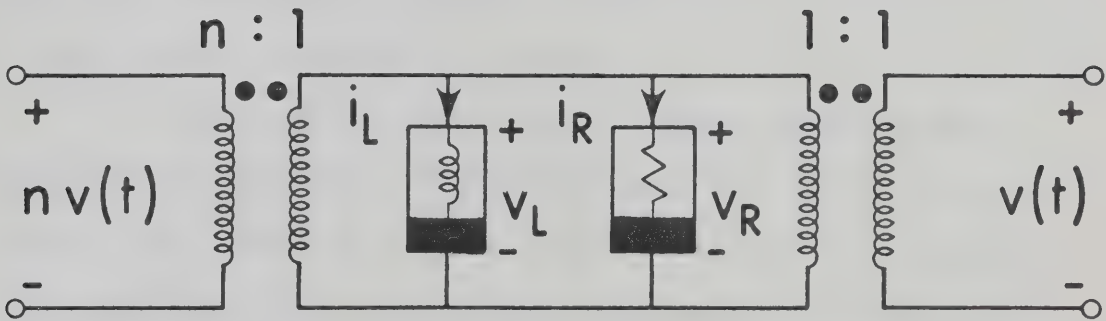


FIG. 2.2

Lumped circuit model for an iron-core transformer

$\lambda(t)$ is the flux linking this winding. This is the circuit model that is used in the analysis of the magnetic amplifiers.

2.3 Determination of $f(\cdot)$ and $g(\cdot)$

Since the model was found to exhibit most of the important properties observed in practice [8]. Hence if $f(\cdot)$ and $g(\cdot)$ are identified to simulate the hysteresis loop of the iron-core inductor under consideration, then it is reasonable to assume that the model will give realistic results under any type of excitation. The type of excitation is dependent on the system in which the iron-core inductor or transformer is imbedded. To identify $f(\cdot)$ and $g(\cdot)$ a pair of waveforms $i(t)$, $\lambda(t)$ must be measured. The nonlinearity of the model implies that there is no apparent advantage of one set of measurement over the other. Thus, the obvious choice is to use a set of measurements that can easily lead to the identification of the nonlinear functions $f(\cdot)$ and $g(\cdot)$.

Since the iron cores used in magnetic amplifier have symmetric hysteresis loops, the two functions $f(\cdot)$ and $g(\cdot)$ are odd functions [8]. Assuming a cosine like variation of $\lambda(t)$, a sinusoidal test signal being used to produce the hysteresis loop, then $\lambda(t)$ is an even function of time while its derivative $\lambda'(t) = \frac{d\lambda}{dt}$ is an odd function of time. Since $f(\cdot)$ and $g(\cdot)$ are odd functions,

$$f(\lambda(-t)) = -f(\lambda(t)) \quad (2.4)$$

$$g^{-1}(\lambda'(-t)) = -g^{-1}(\lambda'(t)) \quad (2.4)$$

Thus $f(\lambda(t))$ is an even function of time while $g^{-1}(\lambda'(t))$ is an odd function of time. If equation (2.1) is rearranged in the form

$$i(t) = g^{-1}(\lambda'(t)) + f(\lambda(t)) \quad (2.5)$$

and the current $i(t)$ is expressed as the sum of an even component $i_e(t)$ and an odd component $i_o(t)$ where,

$$i_e(t) = \frac{i(t) + i(-t)}{2} \quad (2.6)$$

$$i_o(t) = \frac{i(t) - i(-t)}{2}$$

Then, equations (2.4), (2.5) and (2.6) show that

$$i_e(t) = f(\lambda(t)) \quad (2.7)$$

$$i_o(t) = g^{-1}(\lambda'(t)) \quad (2.8)$$

For $\lambda(t)$ a cosine function of time, there are two instants t_1 and t_2 in each cycle at which

$$\lambda = \lambda(t_1) = \lambda(t_2) \quad (2.9)$$

$$\lambda' = \lambda'(t_1) = -\lambda'(t_2) \quad (2.10)$$

Equations (2.7) to (2.10) give

$$i_e(t_2) = f(\lambda(t_2)) = f(\lambda(t_1)) = i_e(t_1) = i_e \quad (2.11)$$

$$i_o(t_2) = g^{-1}(\lambda'(t_2)) = -g^{-1}(\lambda'(t_1)) = -i_o(t_1) \quad (2.12)$$

But

$$i(t_1) = i_o(t_1) + i_e(t_1) \quad (2.13)$$

$$i(t_2) = i_o(t_2) + i_e(t_2) \quad (2.14)$$

From (2.11) and (2.12) equation (2.14) becomes

$$i(t_2) = -i_o(t_1) + i_e(t_1) \quad (2.15)$$

Thus from (2.13) and (2.15) $f(\lambda)$ and $g^{-1}(\lambda')$ can be related to $i(t_1)$ and $i(t_2)$ as follows,

$$f(\lambda) = f(\lambda(t_1)) = i_e(t_1) = \frac{i(t_1) + i(t_2)}{2} = i_e \quad (2.16)$$

$$g^{-1}(\lambda') = g^{-1}(\lambda'(t_1)) = i_o(t_1) = \frac{i(t_1) - i(t_2)}{2} = \pm d \quad (2.17)$$

In equation (2.17) $d = \left| \frac{i(t_1) - i(t_2)}{2} \right|$ and the use of either the positive or negative sign is dependent on the value of λ' . Since $g(\cdot)$ is a strictly monotonically increasing function and $g(0) = 0$ then

$$g^{-1}(\lambda') = +d \quad \text{for } \lambda' > 0$$

$$g^{-1}(\lambda') = -d \quad \text{for } \lambda' < 0$$

Equations (2.16) and (2.17) show that through a set of measurements and using these two equations the two functions $f(\cdot)$ and $g(\cdot)$ can be completely defined. Thus to determine $f(\cdot)$ and $g(\cdot)$ the hysteresis loop is obtained using the sinusoidal test signal. For each value of λ a horizontal line is drawn intersecting the hysteresis loop at two points corresponding to currents $i(t_1)$, $i(t_2)$, t_1 and t_2 being the two instants at which $\lambda(t_1) = \lambda(t_2)$ and equal to the specific value of λ considered. The value of the current i_e is calculated as the average of $i(t_1)$ and $i(t_2)$ while d is half the magnitude of the difference between them. If this process is repeated, for values of λ spanned by the hysteresis loop, the dashed line in Fig. 2.3 is obtained which lies midway between the locus of $i(t_1)$ and $i(t_2)$. This dashed line represents the relation $\lambda = f^{-1}(i_e)$, and the nonlinear function $f(\cdot)$ is defined. For each value of λ considered the value

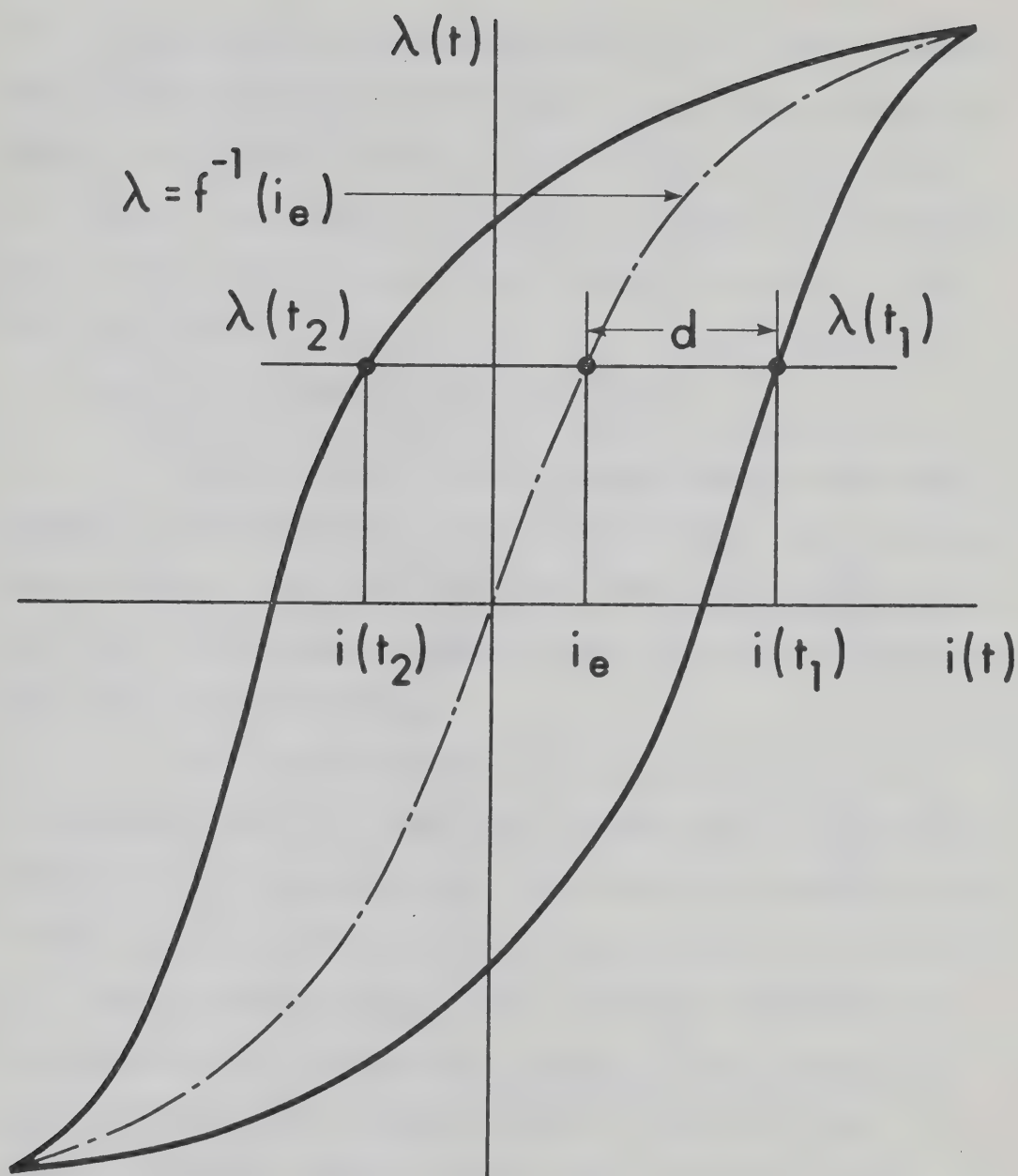


FIG. 2.3

Construction procedure for determining the restoring function $f(\cdot)$ and the dissipation function $g(\cdot)$

of λ' is known and the corresponding value of d is already obtained. Thus the relation between d and λ' can be plotted which completely defines the nonlinear function $g(\cdot)$ as in equation (2.17). Once $f(\cdot)$ and $g(\cdot)$ are defined, this completely defines the characteristics of the nonlinear inductor and resistor in the model of the iron-core transformer.

2.4 Model for the magnetic amplifier cores

The parallel and series connected magnetic amplifiers analyzed in the present work both use two saturable reactors having a common control winding. The circuit model for these two saturable reactors with their three windings is shown in Fig. 2.4, where the transformers shown are ideal transformers.

Since the two saturable reactors are identical the two nonlinear inductors L_1 and L_2 are the same and the two nonlinear resistors R_1 and R_2 are the same. To determine the characteristics of these nonlinear resistors and inductors the dissipation function $g(\cdot)$ and the restoring function $f(\cdot)$ should be identified. The hysteresis loop was experimentally obtained. Then following the steps described in the previous section $f(\cdot)$ and $g(\cdot)$ were obtained. The steps predescribed were used to calculate data points on the nonlinear characteristics of $f(\cdot)$ and $g(\cdot)$. In the present work these steps were carried out at eight values of λ . These eight values of λ were chosen so that the whole range of

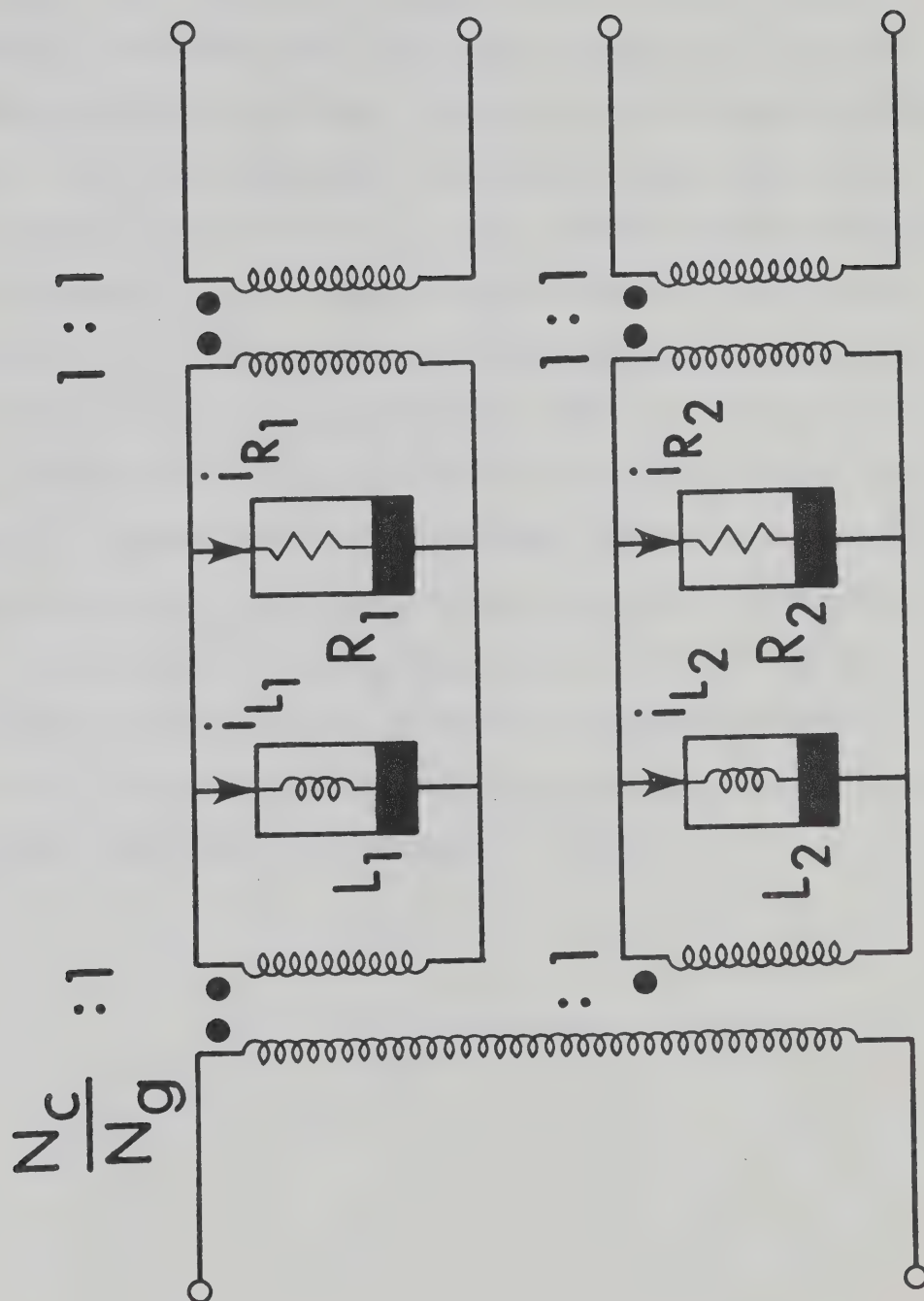


FIG. 2.4

Lumped circuit model for two cores with common control winding

variation of λ is covered, from negative saturation up to positive saturation. Thus eight data points were obtained on the nonlinear characteristics of the nonlinear inductor and the nonlinear resistor, Table 2.1: In order to calculate intermediate points some interpolation method must be used [12]. Due to certain reasons discussed later in Chapter 3, it was found that the piecewise linearization technique has to be used to obtain intermediate points, between the eight data points, on the characteristic curves of the nonlinear inductor and resistor. Thus the nonlinear characteristic curves were replaced by piecewise linear characteristic. These piecewise linear characteristics were then used to calculate and plot the hysteresis loop. The resulting hysteresis loop is shown in Fig. 2.5 which clearly agrees with the actual experimental hysteresis loop shown in Fig. 2.6. In both figures the vertical scale is 0.01 Weber/division and the horizontal scale is 0.03 ampere / division.

Nonlinear Resistors

i (mA)	v (Volts)
-20.5	-39.0
-18.0	-20.0
-14.0	- 5.0
-12.5	- 0.5
12.5	0.5
14.0	5.0
18.0	20.0
20.5	39.0

Nonlinear Inductors

i (mA)	λ (m Wb)
-14.0	-34.0
- 4.0	-33.95
- 2.75	-32.5
- 1.1	-25.0
1.1	25.0
2.75	32.5
4.0	33.95
14.0	34.0

TABLE 2.1

Characteristics of Nonlinear Elements

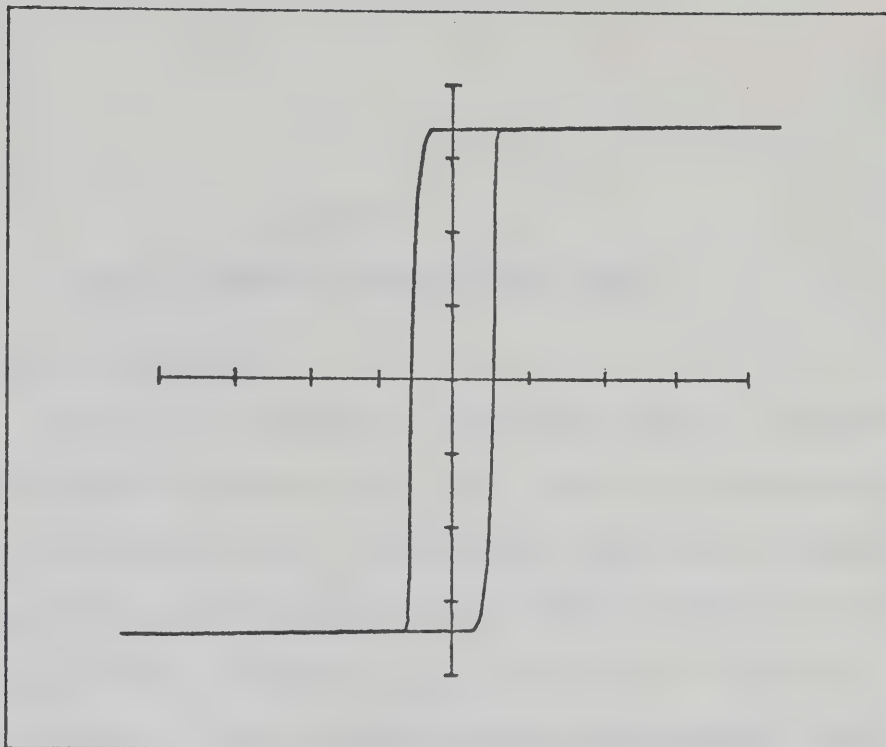


FIG. 2.5

Hysteresis loop computed using the lumped circuit model

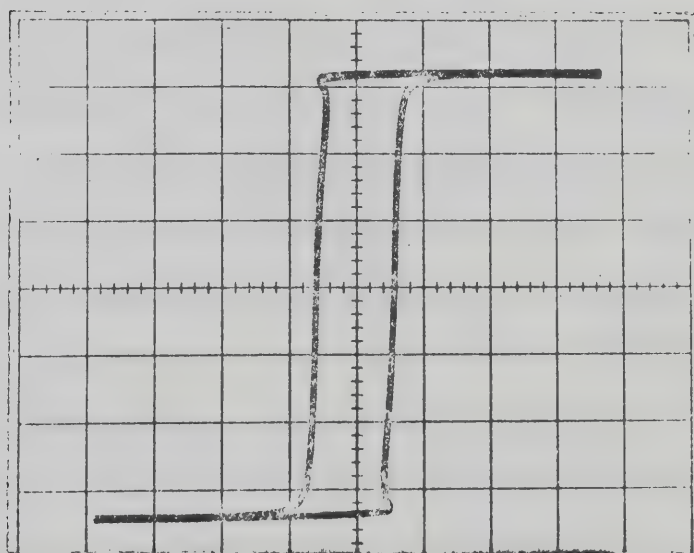


FIG. 2.6

Experimental hysteresis loop

CHAPTER 3

PARALLEL-CONNECTED MAGNETIC AMPLIFIER

3.1 Theory of operation

The circuit diagram of a parallel-connected non-feedback magnetic amplifier is shown in Fig. 3.1. This is an elementary but practical circuit [10-11-13]. As mentioned previously in Chapter 2 the two saturable reactors have a single control winding of N_C turns. This control winding is common to the gate windings of the two saturable reactors. The two gate windings, each having N_g turns, are connected in parallel in such a way that a voltage applied to their parallel connection will, theoretically if $R_{g_1} = R_{g_2}$, induce no a.c. current in the control circuit. The two, parallel-connected, gate windings are in series with a resistive load R_L and in series with an a.c. voltage source e_s . The magnetic amplifier output is the a.c. voltage across the load R_L . If a d.c. output is required, a bridge rectifier can be used. The rectifiers do not affect the operation or the analysis of the magnetic amplifier and are merely considered as a part of the load. The control winding N_C is in series with the d.c. control voltage E_C and in series with a large resistor. The resistance R_C is the sum of the d.c. control winding resistance plus that of the series large resistor. The large value of R_C helps to reduce the value of the a.c. current induced in

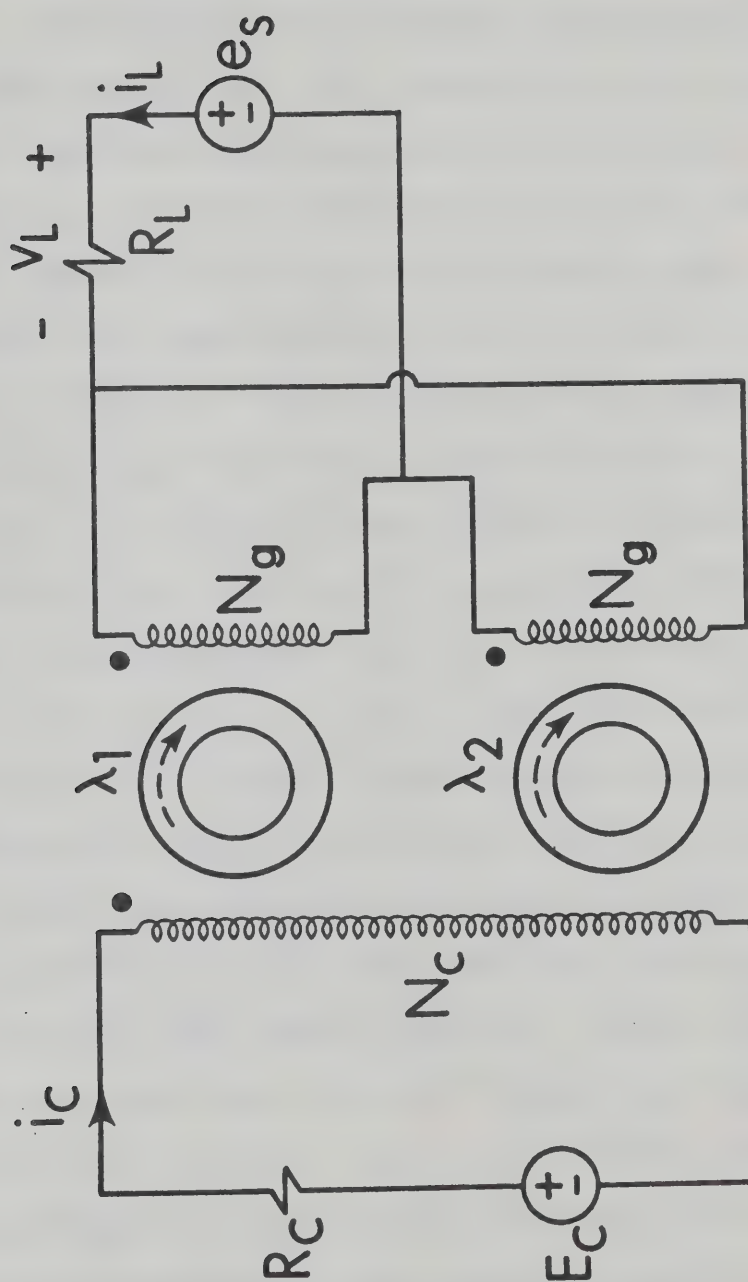


FIG. 3.1

Parallel-connected magnetic amplifier

the control circuit by transformer action.

For $E_C=0$ the control winding contributes no d.c. flux to the cores and the total flux in each of the cores is produced by the a.c. current only and is much less than the value of the flux at saturation. Therefore, the permeabilities of the cores and hence the input impedances of the two gate windings are high compared to R_L and only a very small portion of the a.c. voltage e_s appears across R_L . For $E_C \neq 0$, there is some d.c. flux linkage in each of the two windings due to the d.c. control current i_C . There is also some a.c. flux linkage in each of the two windings due to the a.c. current in the load circuit. In each half of the cycle one of the two gate windings will have the d.c. flux linkage in it due to i_C add to that due to the a.c. load current and the total flux linkage in this winding is driven towards the saturation value. This winding will have a lower inductive impedance than when E_C was zero. In the other winding the two fluxes will oppose and its total flux will still be away from saturation value and this winding will still have a high inductive impedance. Actually the low impedance gate takes most of the load current resulting in further reduction of its impedance. Since the two windings are in parallel, the input impedance of their parallel connection during this first half cycle will be lower than their parallel impedance when E_C was zero. In the next half cycle each of the two windings replaces the other in action. Thus the input impedance of the two parallel-connected

gate windings remains very low over the whole cycle at a value dependent on the magnitude of E_C . This causes an increase of the a.c. load voltage across R_L and hence an increase of the a.c. power delivered to it to values dependent on E_C .

3.2 Analysis

The first step in the analysis of this circuit is to replace the two iron-core transformers shown in Fig. 3.1 with their equivalent nonlinear lumped circuit model shown in Fig. 2.4. The characteristics of the nonlinear elements of this lumped circuit were obtained in the previous chapter. Thus the parallel-connected magnetic amplifier is represented as in Fig. 3.2. All the transformers shown in Fig. 3.2 are ideal transformers. The equivalent circuit of the parallel-connected magnetic amplifier is simplified by referring all the circuit elements to the load side with the necessary variation in the parameters, Fig. 3.3. Rearranging the equivalent circuit and converting all voltage sources to current sources, the equivalent circuit takes the form shown in Fig. 3.4 where,

$$v_C = v_1 \quad (3.1)$$

v_1 is the voltage across the nonlinear inductor L_1 due to variation in the flux λ_1 linking the first gate winding, $v_1 = \frac{d\lambda_1}{dt}$,

$$v_d = -v_2 \quad (3.2)$$

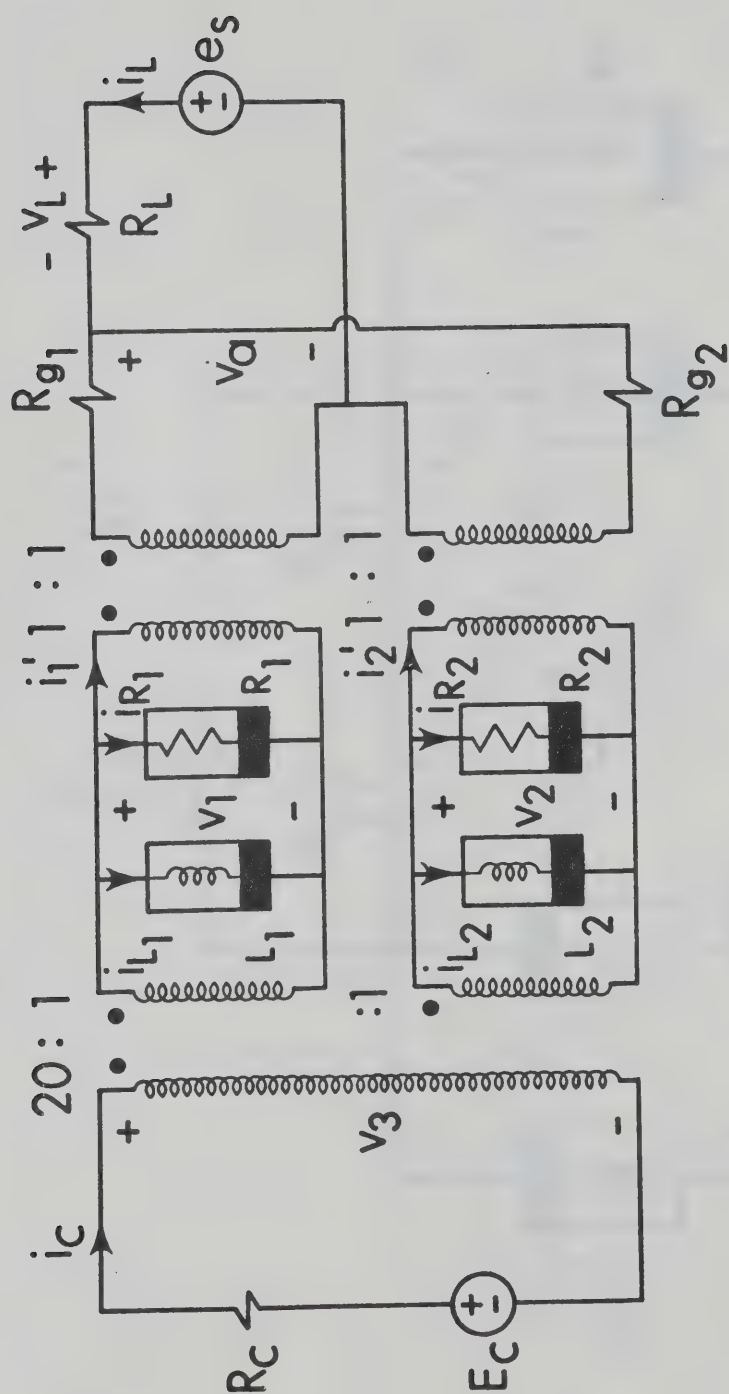


FIG. 3.2

The equivalent circuit of parallel-connected magnetic amplifier using the nonlinear lumped circuit model

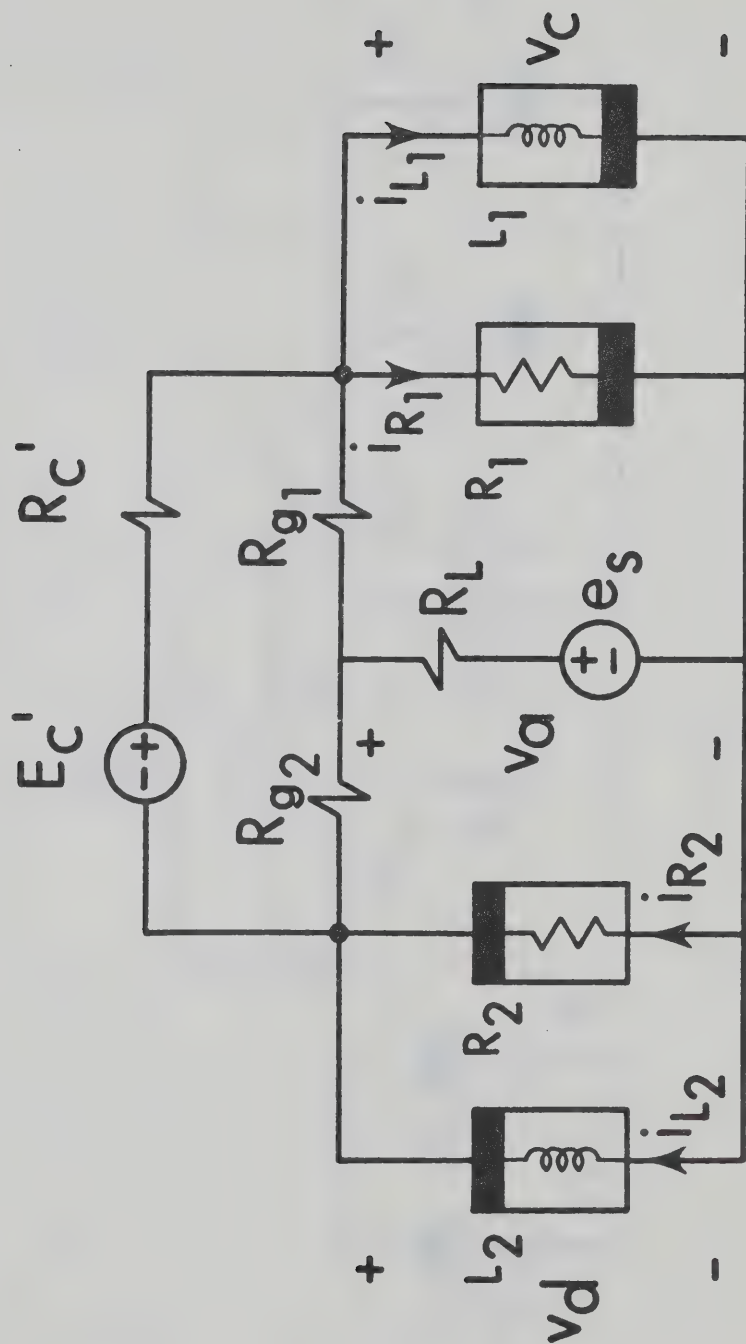


FIG. 3.3

The equivalent circuit for the parallel-connected magnetic amplifier after referring all the circuit elements to the load side

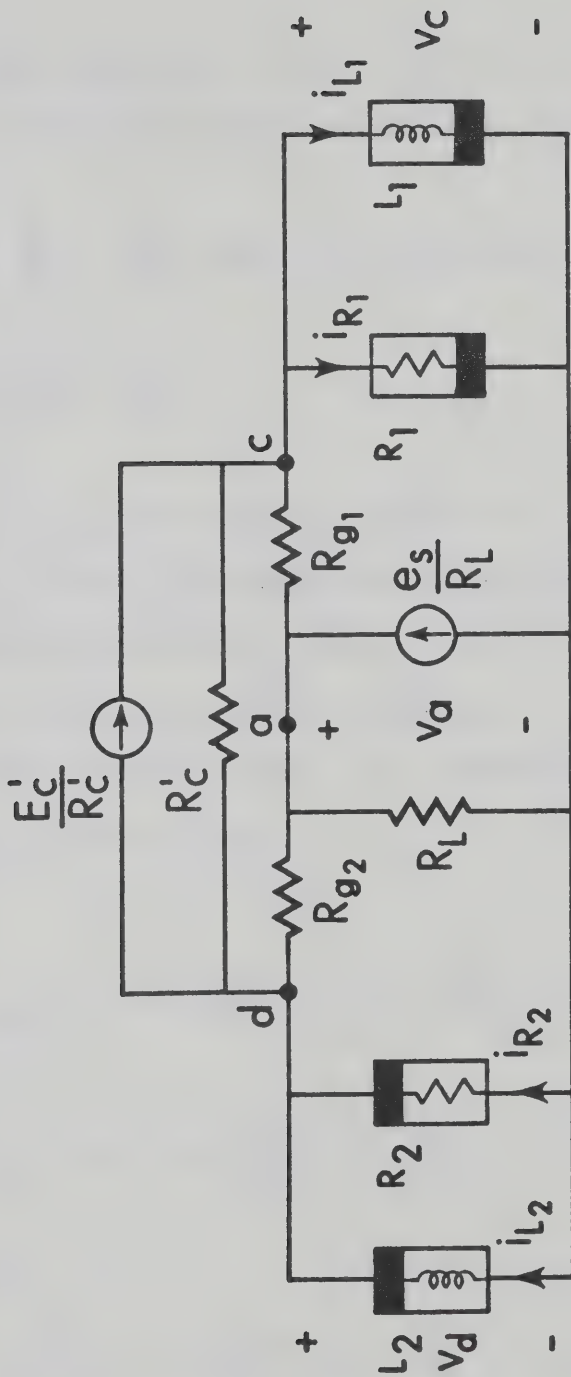


FIG. 3.4

The final equivalent circuit of the parallel-connected magnetic amplifier

v_2 is the voltage across the nonlinear inductor L_2 due to variation in the flux λ_2 linking the second gate winding, $v_2 = \frac{d\lambda_2}{dt}$,

$$E'_C = E_C \frac{N_g}{N_C} = \frac{E_C}{20}, \text{ since } \frac{N_g}{N_C} = \frac{1}{20} \text{ in this case.}$$

$$R'_C = R_C \left(\frac{N_g}{N_C} \right)^2 = \frac{R_C}{400}$$

$e_s = E_s \sin \omega t$, the frequency of this a.c. source is 60 Hz.

The currents i_{L_1} and i_{L_2} are those through the nonlinear inductors L_1 and L_2 respectively while i_{R_1} and i_{R_2} are the currents through the nonlinear resistors R_1 and R_2 respectively.

With reference to Fig. 3.4, applying Kirchhoff current law to nodes c, d and a gives

$$\frac{E'_C}{R'_C} - i_{R_1} - i_{L_1} = v_c \left(\frac{1}{R'_C} + \frac{1}{R_{g_1}} \right) - v_a \left(\frac{1}{R_{g_1}} \right) - v_d \left(\frac{1}{R'_C} \right) \quad (3.3)$$

$$- \frac{E'_C}{R'_C} + i_{R_2} + i_{L_2} = -v_c \left(\frac{1}{R'_C} \right) - v_a \left(\frac{1}{R_{g_2}} \right) + v_d \left(\frac{1}{R'_C} + \frac{1}{R_{g_2}} \right) \quad (3.4)$$

$$\frac{e_s}{R_L} = -v_c \left(\frac{1}{R_{g_1}} \right) + v_a \left(\frac{1}{R_{g_1}} + \frac{1}{R_{g_2}} + \frac{1}{R_L} \right) - v_d \left(\frac{1}{R_{g_2}} \right) \quad (3.5)$$

But from chapter 2 the nonlinear inductors and resistors L_1, L_2, R_1 and R_2 are characterized by

$$\left. \begin{aligned} i_{L_1} &= f(\lambda_1) \\ i_{L_2} &= f(\lambda_2) \end{aligned} \right\} \quad (3.6)$$

and

$$\left. \begin{aligned} v_1 &= g(i_{R_1}) \\ v_2 &= g(i_{R_2}) \end{aligned} \right\} \quad (3.7)$$

Taking the inverse of equations (3.7) the characteristic equations of the two nonlinear resistors take the form

$$\left. \begin{aligned} i_{R_1} &= g^{-1}(v_1) = h(v_1) \\ i_{R_2} &= g^{-1}(v_2) = h(v_2) \end{aligned} \right\} \quad (3.8)$$

where

$$h(\cdot) = g^{-1}(\cdot) \quad (3.9)$$

Substituting equations (3.1) and (3.2) into (3.5) gives

$$\frac{e_s}{R_L} = v_a \left(\frac{1}{R_{g_1}} + \frac{1}{R_{g_2}} + \frac{1}{R_L} \right) - v_1 \left(\frac{1}{R_{g_1}} \right) + v_2 \left(\frac{1}{R_{g_2}} \right) \quad (3.10)$$

Thus

$$v_a = R_t \left[\frac{e_s}{R_L} + \frac{v_1}{R_{g_1}} - \frac{v_2}{R_{g_2}} \right] \quad (3.11)$$

where

$$R_t = \left[\frac{1}{\frac{1}{R_{g_1}} + \frac{1}{R_{g_2}} + \frac{1}{R_L}} \right] \quad (3.12)$$

Substituting equations (3.1), (3.2), (3.6) and (3.8) into (3.3) and (3.4) gives

$$\begin{aligned} \frac{E'_C}{R'_C} - h(v_1) - f(\lambda_1) &= v_1 \left(\frac{1}{R'_C} + \frac{1}{R_{g_1}} \right) - \frac{R_t}{R_{g_1}} \left(\frac{e_s}{R_L} + \frac{v_1}{R_{g_1}} - \frac{v_2}{R_{g_2}} \right) \\ &\quad + \frac{v_2}{R'_C} \end{aligned} \quad (3.13)$$

$$\begin{aligned} \frac{E'_C}{R'_C} - h(v_2) - f(\lambda_2) &= v_1 \left(\frac{1}{R'_C} \right) + \frac{R_t}{R_{g_2}} \left(\frac{e_s}{R_L} + \frac{v_1}{R_{g_1}} - \frac{v_2}{R_{g_2}} \right) + \\ &\quad v_2 \left(\frac{1}{R_{g_2}} + \frac{1}{R'_C} \right) \end{aligned} \quad (3.14)$$

Equations (3.13) and (3.14) can be rewritten as

$$\begin{aligned} \frac{E'_C}{R'_C} - f(\lambda_1) + \frac{R_t}{R_{g_1}} \frac{e_s}{R_L} &= h(v_1) + v_1 \left(\frac{1}{R'_C} + \frac{1}{R_{g_1}} - \frac{R_t}{(R_{g_1})^2} \right) + \\ &\quad v_2 \left(\frac{1}{R'_C} + \frac{R_t}{R_{g_1} R_{g_2}} \right) \end{aligned} \quad (3.15)$$

$$\frac{E'_C}{R'_C} - f(\lambda_2) - \frac{R_t}{R_{g_2}} \frac{e_s}{R_L} = h(v_2) + v_1 \left(\frac{1}{R'_C} + \frac{R_t}{R_{g_1} R_{g_2}} \right) + v_2 \left(\frac{1}{R'_C} + \frac{1}{R_{g_2}} - \frac{R_t}{(R_{g_2})^2} \right) \quad (3.16)$$

Putting $v_1 = \frac{d\lambda_1}{dt}$ and $v_2 = \frac{d\lambda_2}{dt}$ equations (3.15) and (3.16) take the form

$$\frac{E'_C}{R'_C} - f(\lambda_1) + \frac{R_t}{R_{g_1}} \frac{e_s}{R_L} = F_2 \left(\frac{d\lambda_1}{dt} \right) + \frac{d\lambda_2}{dt} \left(\frac{1}{R'_C} + \frac{R_t}{R_{g_1} R_{g_2}} \right) \quad (3.17)$$

$$\frac{E'_C}{R'_C} - f(\lambda_2) - \frac{R_t}{R_{g_2}} \frac{e_s}{R_L} = F_3 \left(\frac{d\lambda_2}{dt} \right) + \frac{d\lambda_1}{dt} \left(\frac{1}{R'_C} + \frac{R_t}{R_{g_1} R_{g_2}} \right) \quad (3.18)$$

where,

$$F_2 \left(\frac{d\lambda_1}{dt} \right) = h(v_1) + v_1 \left(\frac{1}{R'_C} + \frac{1}{R_{g_1}} - \frac{R_t}{(R_{g_1})^2} \right)$$

$$F_3 \left(\frac{d\lambda_2}{dt} \right) = h(v_2) + v_2 \left(\frac{1}{R'_C} + \frac{1}{R_{g_2}} - \frac{R_t}{(R_{g_2})^2} \right)$$

Examination of the two differential equations (3.17) and (3.18) show

that, except for the difference between $F_2(\cdot)$ and $F_3(\cdot)$, $R_{g_1} \neq R_{g_2}$, the two equations look the same except that in one half cycle $\frac{E'_C}{R'_C}$ adds to $\frac{R_t}{R_{g_1}} \frac{e_s}{R_L}$ in the first equation while it opposes $\frac{R_t}{R_{g_2}} \frac{e_s}{R_L}$

in the second and this action is reversed in the next half cycle. Actually this is the same as saying that in one half cycle the flux due to E_C adds to the a.c. flux in the first winding and opposes that in the second and the situation is reversed in the next half cycle.

The two differential equations are nonlinear and have no analytical solution. In order to use the digital computer to obtain a numerical solution it is necessary to formulate these differential equations in the normal form [12].

$$\frac{d\mathbf{X}}{dt} = \mathbf{f}(\mathbf{X}, t) \quad (3.19)$$

Virtually all numerical techniques for solving a sequence of nonlinear differential equations are for those in such normal form. So, in order to use any of these numerical techniques it is necessary to put equations (3.17) and (3.18) in the normal form. This means putting $\frac{d\lambda_1}{dt}$ and $\frac{d\lambda_2}{dt}$ as two explicit functions of λ_1 , λ_2 and time t in the form

$$\frac{d\lambda_1}{dt} = f_4(\lambda_1, \lambda_2, t) \quad (3.20)$$

$$\frac{d\lambda_2}{dt} = f_5 (\lambda_1, \lambda_2, t) \quad (3.21)$$

Since both $F_2 \left(\frac{d\lambda_1}{dt} \right)$ and $F_3 \left(\frac{d\lambda_2}{dt} \right)$ are nonlinear functions, $\frac{d\lambda_1}{dt}$ and $\frac{d\lambda_2}{dt}$ cannot be put in the form of equations (3.20) and (3.21).

The nonlinearities of $F_2(\cdot)$ and $F_3(\cdot)$ result from the two nonlinear resistors R_1 and R_2 .

As mentioned before in chapter 2 only eight data points are available on the characteristics of the nonlinear resistors R_1 and R_2 . For calculating intermediate points an interpolation method must be used. The piecewise-linearization technique is one of these methods. The use of this method, unlike other interpolation techniques, makes it possible to put equations (3.15) and (3.16) in the required normal form. Applying this piecewise-linearization technique the $v - i$ characteristic curve of each of the two nonlinear resistors is replaced with a number of linear segments with the eight data points coinciding with the break points, Fig. 3.5(b). Hence, the characteristic equations of the two resistors R_1 and R_2 take the form, [APP.A],

$$i_{R_1} = h(v_1) = \sum_{K=1}^7 G_K v_1 + \sum_{K=1}^7 I_K, \quad K = 1, 2, \dots, 7 \quad (3.22)$$

$$i_{R_2} = h(v_2) = \sum_{m=1}^7 G_m v_2 + \sum_{m=1}^7 I_m, \quad m = 1, 2, \dots, 7 \quad (3.23)$$

Substituting these expressions for $h(v_1)$ and $h(v_2)$ in (3.15),

(3.16) and rearranging give

$$\begin{bmatrix} \frac{E'_C}{R'_C} - f(\lambda_1) + \frac{R_t}{R_{g_1}} \frac{E_s \sin \omega t}{R_L} - K I_1 \\ \frac{E'_C}{R'_C} - f(\lambda_2) - \frac{R_t}{R_{g_2}} \frac{E_s \sin \omega t}{R_L} - m I_2 \end{bmatrix} = \begin{bmatrix} T_P \end{bmatrix} \begin{bmatrix} v_1 \\ v_2 \end{bmatrix} \quad (3.24)$$

where

$$\begin{bmatrix} T_P \end{bmatrix} = \begin{bmatrix} K G_1 + \frac{1}{R'_C} + \frac{1}{R_{g_1}} - \frac{R_t}{(R_{g_1})^2} & \frac{1}{R'_C} + \frac{R_t}{R_{g_1} R_{g_2}} \\ \frac{1}{R'_C} + \frac{R_t}{R_{g_1} R_{g_2}} & m G_2 + \frac{1}{R'_C} + \frac{1}{R_{g_2}} - \frac{R_t}{(R_{g_2})^2} \end{bmatrix} \quad (3.25)$$

Thus

$$\begin{aligned} v_1 = \frac{d\lambda_1}{dt} = \frac{1}{|T_P|} & \left\{ \frac{E'_C}{R'_C} \left[m G_2 + \frac{1}{R_{g_2}} - \frac{R_t}{R_{g_2}} \left(\frac{1}{R_{g_2}} + \frac{1}{R_{g_1}} \right) \right] + \right. \\ & \frac{R_t}{R_L} E_s \sin \omega t \left[\frac{m G_2}{R_{g_1}} + \frac{1}{R_{g_1} R_{g_2}} + \frac{1}{R'_C} \left(\frac{1}{R_{g_1}} + \frac{1}{R_{g_2}} \right) \right] - \\ & f(\lambda_1) \left[m G_2 + \frac{1}{R'_C} + \frac{1}{R_{g_2}} - \frac{R_t}{(R_{g_2})^2} \right] + \\ & f(\lambda_2) \left[\frac{1}{R'_C} + \frac{R_t}{R_{g_1} R_{g_2}} \right] - K I_1 \left[m G_2 + \frac{1}{R'_C} + \right. \\ & \left. \left. \frac{1}{R_{g_2}} - \frac{R_t}{(R_{g_2})^2} \right] + m I_2 \left[\frac{1}{R'_C} + \frac{R_t}{R_{g_1} R_{g_2}} \right] \right\} \quad (3.26) \end{aligned}$$

$$\begin{aligned}
 v_2 = \frac{d\lambda_2}{dt} = \frac{1}{|T_p|} & \left\{ \frac{E'_C}{R'_C} \left[K^G_1 + \frac{1}{R_{g_1}} - \frac{R_t}{R_{g_1}} \left(\frac{1}{R_{g_1}} + \right. \right. \right. \\
 & \left. \left. \left. \frac{1}{R_{g_2}} \right) \right] - \frac{R_t}{R_L} E_s \sin \omega t \left[\frac{K^G_1}{R_{g_2}} + \frac{1}{R_{g_1} R_{g_2}} + \right. \right. \\
 & \left. \left. \frac{1}{R'_C} \left(\frac{1}{R_{g_1}} + \frac{1}{R_{g_2}} \right) \right] - f(\lambda_2) \left[K^G_1 + \frac{1}{R'_C} + \right. \right. \\
 & \left. \left. \frac{1}{R_{g_1}} - \frac{R_t}{(R_{g_1})^2} \right] + f(\lambda_1) \left[\frac{1}{R'_C} + \frac{R_t}{R_{g_1} R_{g_2}} \right] - \right. \\
 & m I_2 \left[K^G_1 + \frac{1}{R'_C} + \frac{1}{R_{g_1}} - \frac{R_t}{(R_{g_1})^2} \right] + K I_1 \left[\frac{1}{R'_C} + \right. \\
 & \left. \left. \frac{R_t}{R_{g_1} R_{g_2}} \right] \right\} \quad (3.27)
 \end{aligned}$$

where

$|T_p|$ = determinant of the matrix $[T_p]$.

The values of K and m are dependent on the values of v_1 and v_2 respectively. For all possible combinations of m and K , the determinant $|T_p|$ has a finite non-zero value. To show that the two equations (3.26) and (3.27) have a unique solution that satisfy the initial conditions at $t = 0$, the Cauchy-Lipschitz theorem [14] is used. The two functions $f(\lambda_1)$ and $f(\lambda_2)$ are continuous, single valued functions

of λ_1 and λ_2 respectively. The sinusoidal signal $E_s \sin \omega t$ is also continuous, single valued function for all values of time t . Therefore the right hand sides of equations (3.26) and (3.27) are continuous, single valued functions of λ_1 , λ_2 and t for all values of λ_1 , λ_2 , t and hence satisfy the first condition of the Cauchy-Lipschitz theorem. Moreover these two right hand sides are differentiable functions of λ_1 , λ_2 and t . Therefore these two right hand side functions are Lipschitz functions and hence satisfy the second condition of the Cauchy-Lipschitz theorem. Therefore equations (3.26) and (3.27) have a unique solution for all values of $t \geq 0$. This solution provides λ_1 , λ_2 , v_1 and v_2 as functions of time t . These two differential equations are solved numerically because there is no analytical solution available. As mentioned before the objective is to examine the accuracy of the mathematical model in predicting the performance of the parallel-connected magnetic amplifier. This can only be done by comparing the actual amplitudes and waveforms of the quantities measured experimentally with the corresponding computed amplitudes and waveforms resulting from the mathematical analysis in which the mathematical model is used. Therefore, the quantities to be compared must be experimentally measurable. But the voltages v_1 and v_2 cannot be measured experimentally due to the presence of the finite values of R_{g1} and R_{g2} . Therefore, the experimentally measurable quantities whose waveforms and amplitudes are to be compared with their respective computed waveforms and amplitudes are v_a , the voltage across the two parallel-connected gate windings, and the

load voltage v_L . These voltages are related to v_1 , v_2 and e_s as

$$v_a = R_t \left[\frac{E_s \sin \omega t}{R_L} + \frac{v_1}{R_{g_1}} - \frac{v_2}{R_{g_2}} \right] \quad (3.28)$$

$$v_L = E_s \sin \omega t - v_a \quad (3.29)$$

3.3 Numerical computations

To start numerical computation, using any of the numerical techniques to solve the two differential equations (3.26) and (3.27), it is necessary to know the initial values of λ_1 and λ_2 at $t = 0$, namely, $\lambda_1(0)$ and $\lambda_2(0)$. Before the a.c. voltage source e_s is switched on at $t = 0$, there is no a.c. voltage applied to the circuit and hence there will be no a.c. current flowing through either one of the two gate windings. Under such condition the only flux in the two cores will be the d.c. flux produced by the d.c. current flowing through the control winding therefore,

$$v_1 \Big|_{t=0} = \frac{d\lambda_1}{dt} \Big|_{t=0} = 0$$

$$v_2 \Big|_{t=0} = \frac{d\lambda_2}{dt} \Big|_{t=0} = 0$$

Then

$$\lambda_1(0) = C_1$$

$$\lambda_2(0) = C_2$$

The values of the constants C_1 and C_2 are dependent on the currents flowing through the two inductors L_1 and L_2 respectively at $t=0$.

Since $v_1(0) = v_2(0) = 0$ then from the characteristics of the resistors R_1 and R_2 , Fig. 3.5(b).

$$i_{R_1}(0) = i_{R_2}(0) = 0$$

also

$$i_C(0) = \frac{E_C}{R_C}$$

and

$$i_1' = i_2' = 0$$

All these imply that the initial currents through the inductors L_1 and L_2 are

$$i_{L_1} = i_{L_2} = 20 i_C = 20 \frac{E_C}{R_C}$$

The characteristics of the two inductors show that the corresponding initial flux $\lambda_1(0)$ and $\lambda_2(0)$ are

$$\lambda_1(0) = \lambda_2(0) = f^{-1} \left(20 \frac{E_C}{R_C} \right)$$

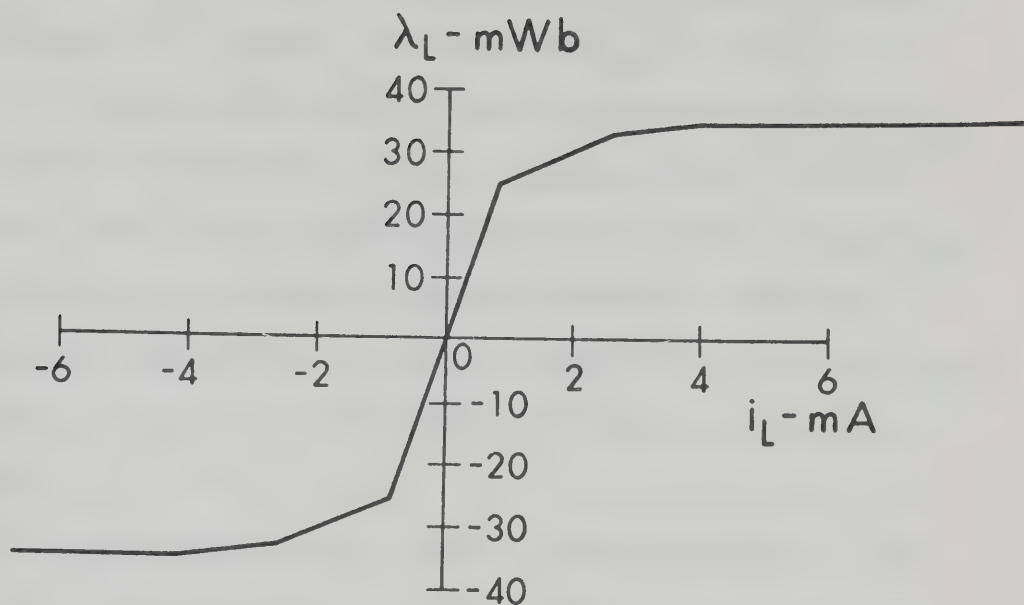
These initial conditions satisfy the two differential equations at $t=0$,

this can be seen from equations (3.15) and (3.16).

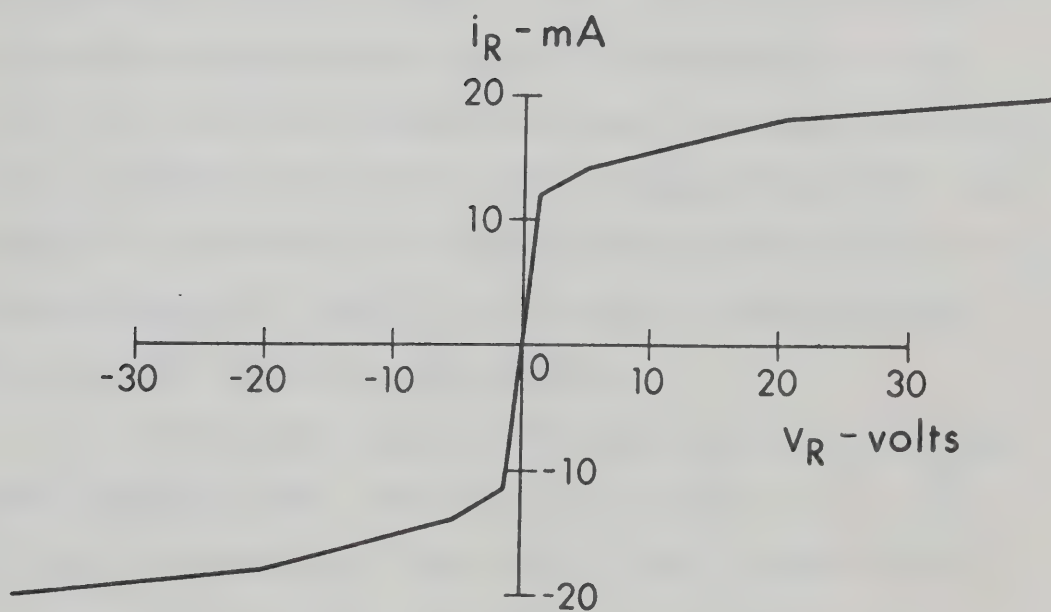
A computer program for solving equations (3.26) and (3.27) was written. This program consists of a main program and four subroutines in addition to the library subroutine HPCG [15].

The library subroutine HPCG is one of the subroutines that can be used to solve a sequence of first order ordinary differential equations with given initial values. This subroutine uses the Hamming predictor-corrector method. This method is not self starting, that is, the functional values at a single previous point are not enough to get the functional values ahead. Therefore, to obtain the starting values, a special Runge-Kutta procedure followed by one iteration step is used added to the predictor-corrector method. The Hamming predictor-corrector method is a stable fourth order integration procedure that requires the evaluation of the right hand side of the sequence of the differential equations only two times per step. This is a great advantage compared with other methods of the same order of accuracy, especially the Runge-Kutta method, which requires the evaluation of the right hand side four times per step. Another advantage is that at each step of calculation procedure this subroutine is able, without a significant amount of calculation time, to choose and change the step size.

The subroutine FCT is one of the external subroutines that should be used with HPCG and it is intended to compute the right



(a)



(b)

FIG. 3.5

The i - λ curve (a) for the nonlinear inductors
and v - i curve (b) for the nonlinear resistors

hand side of the two differential equations (3.26) and (3.27) for given values of t , λ_1 and λ_2 , i.e. calculate $\frac{d\lambda_1}{dt}$ and $\frac{d\lambda_2}{dt}$.

The subroutine AVR is used to determine the operating point on each of the piecewise-linear characteristics of the two resistors R_1 and R_2 corresponding to voltages v_1 and v_2 respectively. This is done by determining the segment on which the operating point lies for each of the two resistors, thus the values of K , m and hence K^G_1 , m^G_2 , K^I_1 and m^I_2 corresponding to the operating point are known.

As in all practical cases the characteristics of each of L_1 and L_2 are known only by a finite number of experimentally obtained data points, in the present work these are eight, and an interpolating subroutine should be used. The subroutine BWLINT is an interpolating subroutine to enable the calculation of values λ_1 and λ_2 on the characteristics of L_1 and L_2 for given values of i_{L_1} and i_{L_2} , and vice versa. This routine consists of only first order terms and is equivalent to a piecewise linear representation for the characteristics of L_1 and L_2 , Fig. 3.5(a), with the data points coinciding with the break points [APP.A].

The second external subroutine required by HPCG is the output subroutine OUTP. This is intended to store λ_1 , λ_2 , $\frac{d\lambda_1}{dt}$, $\frac{d\lambda_2}{dt}$ and t as an array and then to plot v_L and v_a versus time t .

The main program and its subroutines are used to solve equations (3.26) and (3.27), calculate and plot the steady state values of v_a and v_L versus time. This was done for values of E_C equal to 0.0, 5, 10, 15, 20, 25 and 30 volts. The resulting waveforms are shown in Figs. 3.6(a) and (b) to 3.12(a) and (b). The a.c. voltage source e_s has an amplitude equal to 17.5 volts and frequency of 60 Hz . The values of the resistors used in the calculation are exactly equal to those used in the practical circuit of the parallel-connected magnetic amplifier.

3.4 Experimental results

The values of the parameters of the actual parallel-connected magnetic amplifier are

$$e_s = 17.5 \sin (2\pi 60t)$$

$$R_L = 100 \quad \text{ohm}$$

$$R_C = 10189 \quad \text{ohm}$$

$$\frac{N_C}{N_g} = 20$$

$$R_{g_1} = 0.76 \quad \text{ohm}$$

$$R_{g_2} = 0.765 \quad \text{ohm}$$

The values of the d.c. control voltage is taken as 0.0, 5, 10, 15, 20, 25 and 30 volts. For each of these values the steady state waveforms for v_L , the voltage across the load R_L , and v_a , the voltage across the parallel connection of the two gate windings, were photographed. These waveforms are shown in Figs. 3.6(c) and (d) to 3.12(c) and (d) for each of these the time scale was 2.5 ms /division and the voltage scale was 10 volts / division.

3.5 Comparison

The checking of the accuracy of the mathematical model in predicting the accurate performance of the parallel-connected magnetic amplifier is the objective of this section. The waveforms calculated and plotted from the analysis, in which the mathematical model replaces the magnetic iron-cores, are compared with the actual experimental waveforms. This was done for values of E_C equal to 0.0, 5, 10, 15, 20, 25 and 30 volts. The waveforms are shown in Figs. 3.6 to 3.12 where Figs. (a) and Figs. (b) are the waveforms of the load voltage v_L and the gate voltage v_a respectively obtained using the mathematical model while Figs. (c) and Figs. (d) are the actual experimental load voltage v_L and gate voltage v_a waveforms. In all these figures the voltage scale is 10 volts / division and the time scale is 2.5 ms / division.

Fig. 3.6 was obtained for $E_C = 0.0$ volts. It is clear that the waveforms obtained using the mathematical representation are

in good agreement with the experimental waveforms. Actually the only difference is the presence of the sharp points appearing in Fig. 3.6(a) and (b). The sharp points at the maximum and minimum values of the load voltage in Fig. 3.6(a) results in the apparent difference in the amplitude of the waveforms in Fig. 3.6(a) and (c). Concerning the waveforms it is clear that the mathematical model successfully predicts when the gate does or does not take most of the a.c. voltage. Fig. 3.7 was obtained for $E_C = 5$ volts. The duration over which the load takes most of a.c. voltage starts to increase and thus the a.c. power delivered to the load increases. Comparison of Fig. 3.7(a) and (b) with Fig. 3.7(c) and (d) respectively shows that the agreement concerning both amplitudes and waveforms is excellent except for the previously stated difference of the sharp points appearing in Fig. 3.7(a) and (b).

As E_C increases, the duration of time over which the load takes most of the a.c. voltage start to increase. Figs. 3.8, 3.9, 3.10, 3.11 and 3.12 are for E_C equal to 10, 15, 20, 25 and 30 volts respectively. In all these figures it is clear that the mathematical model is very successful in predicting the waveforms of v_L and v_a . Fig. 3.12 was obtained for E_C equal to 30 volts. For this value of E_C , or greater values, the load has all the a.c. voltage across its terminal. This is clear in both Fig. 3.12 (a) and (c). The only difference is that small sharp dip in the load voltage in Fig. 3.12(a)

does not clearly appear in Fig. 3.12(c). The same holds for the small sharp pulse in Fig. 3.12(b) which does not clearly appear in Fig. 3.12(d). This difference may be due to the piecewise linearization technique which causes the slight gradual deformation in the sinusoidal waveforms in Fig. 3.12(c) to appear as a sudden dip in Fig. 3.12(a). Thus, it is clear from the comparison that the mathematical model used in the analysis successfully predicts the performance of the parallel-connected magnetic amplifier with no feedback with the exception of the sharp voltage changes appearing in those waveforms computed using the model. This may be arising from using the piecewise linearization technique, in interpolating the characteristics of L_1 , L_2 , R_1 and R_2 , together with some inaccuracy of the model. The exactness of the model may be improved by inserting some parasitic elements.

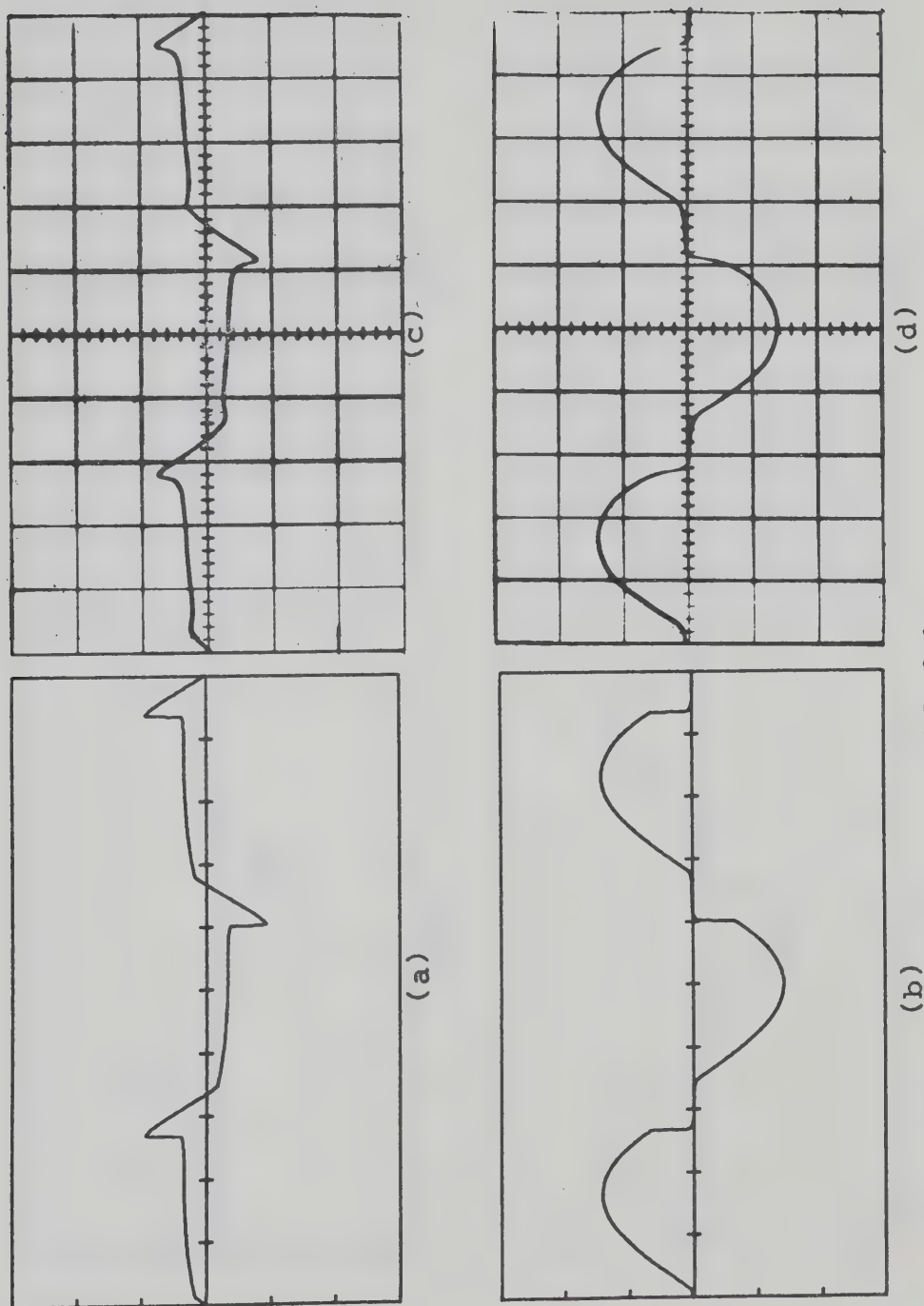


FIG. 3.6
Experimental and computed voltage waveforms for $E_C = 0.0$

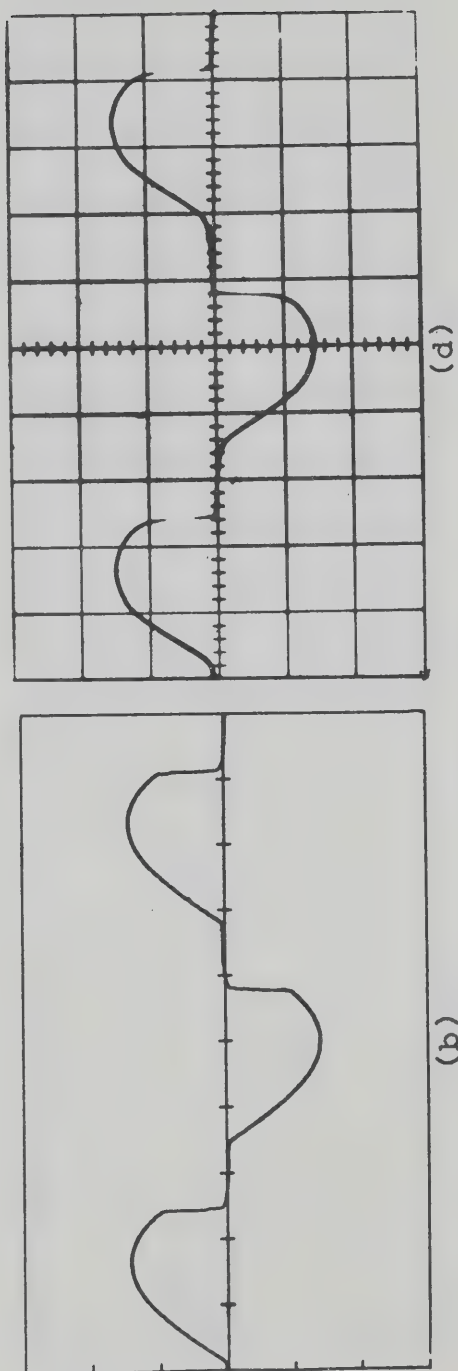
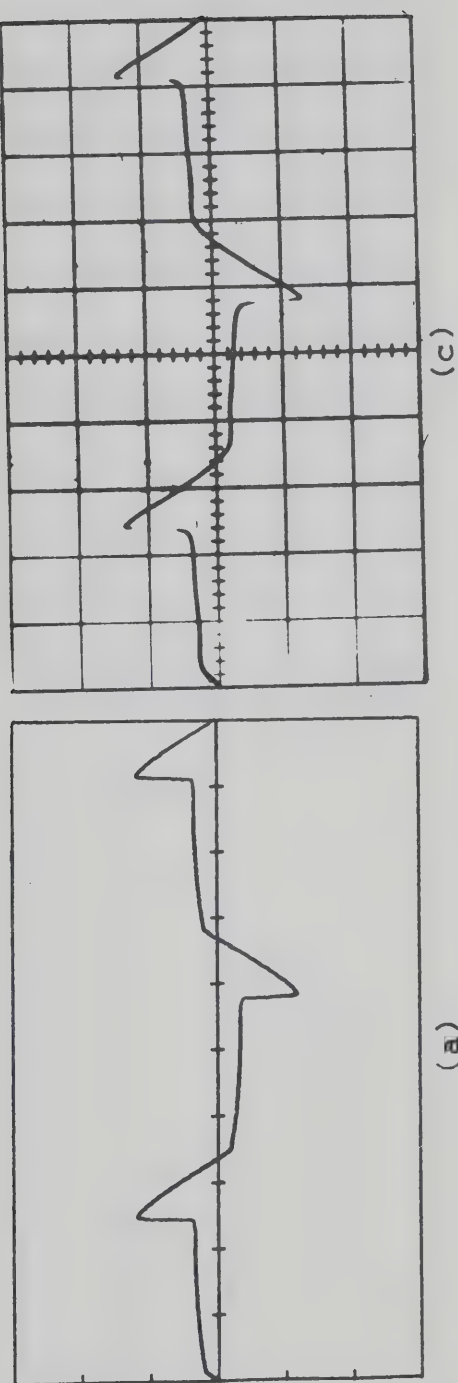


FIG. 3.7

Experimental and computed voltage waveforms for $E_C = 5$

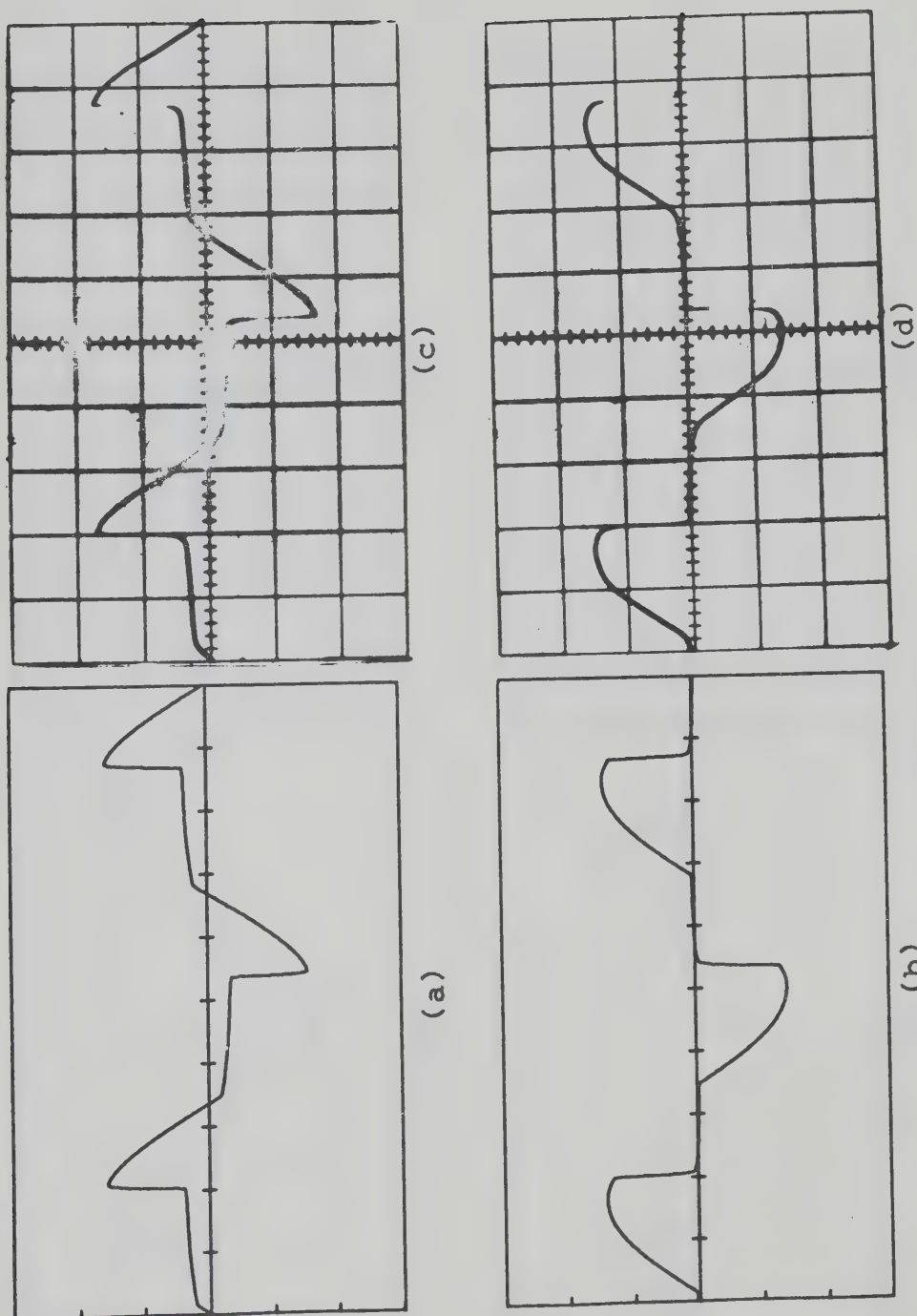


FIG. 3.8
Experimental and computed voltage waveforms for $E_C = 10$

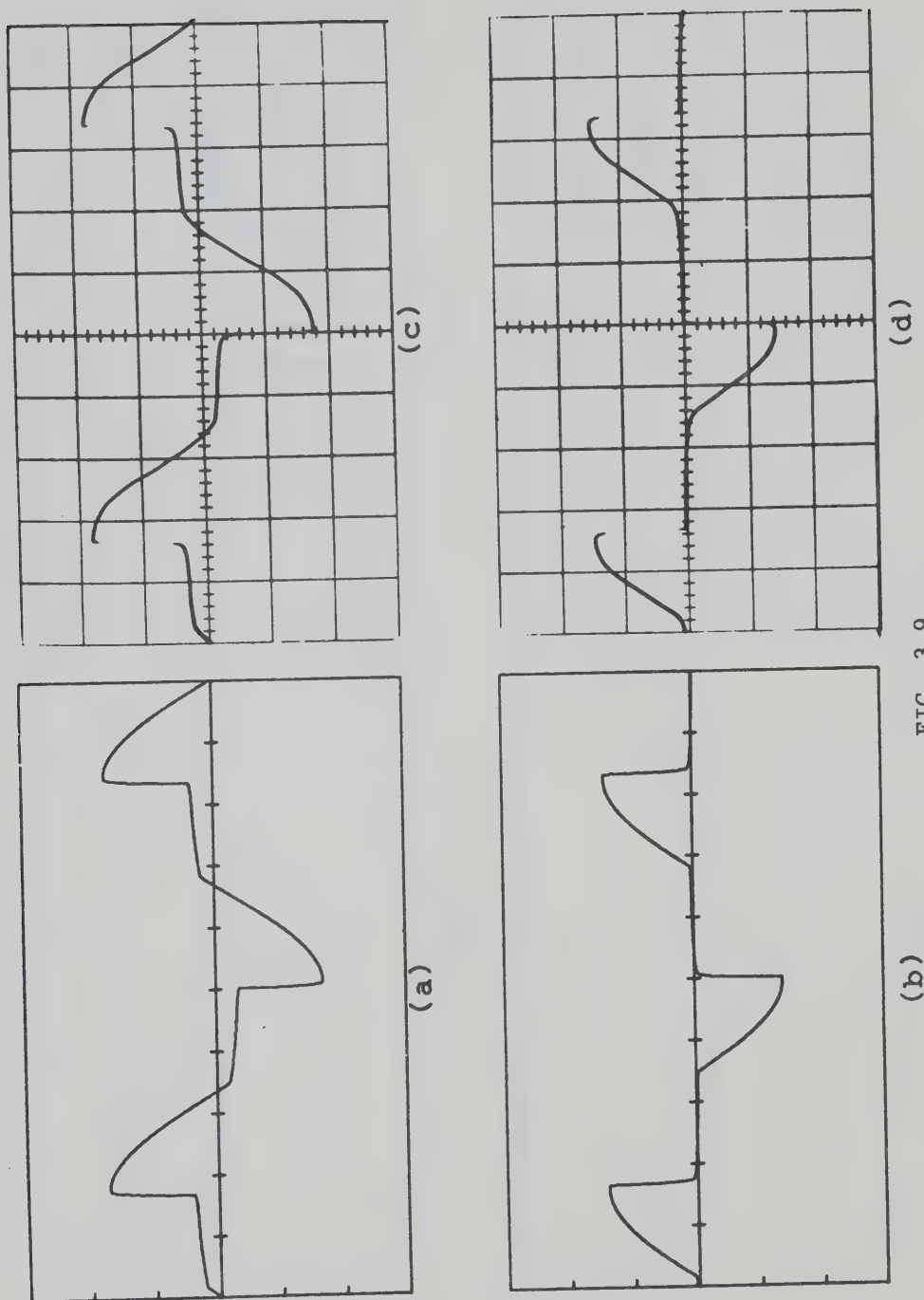
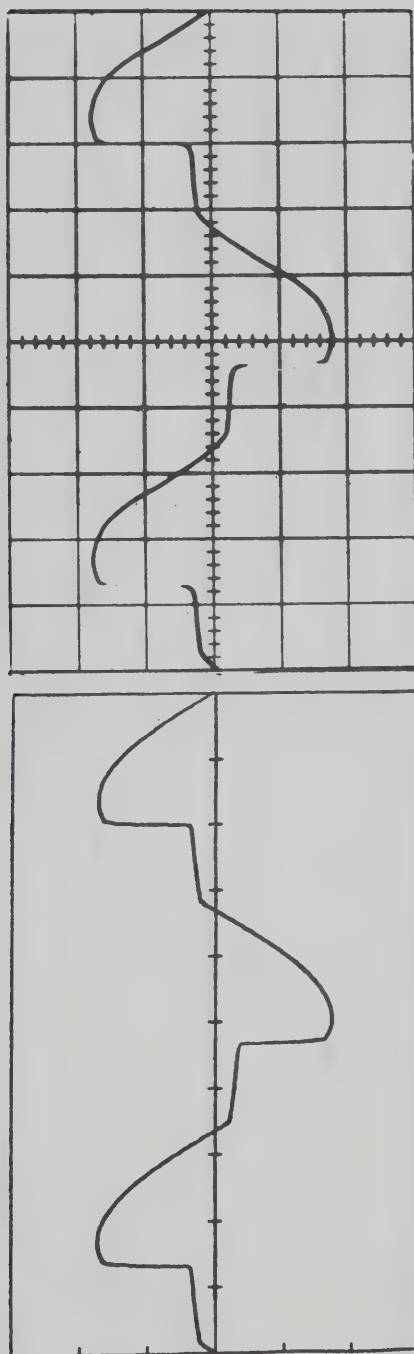
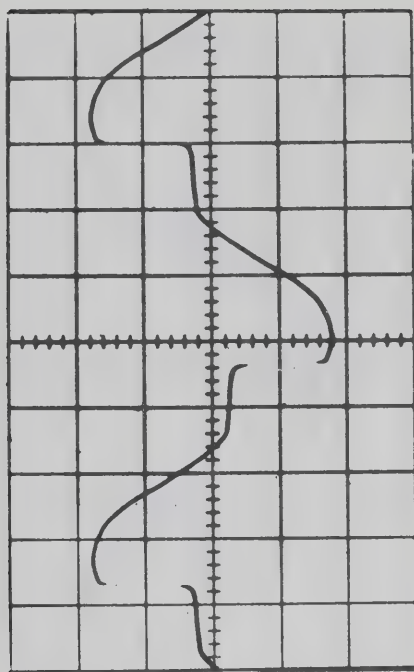


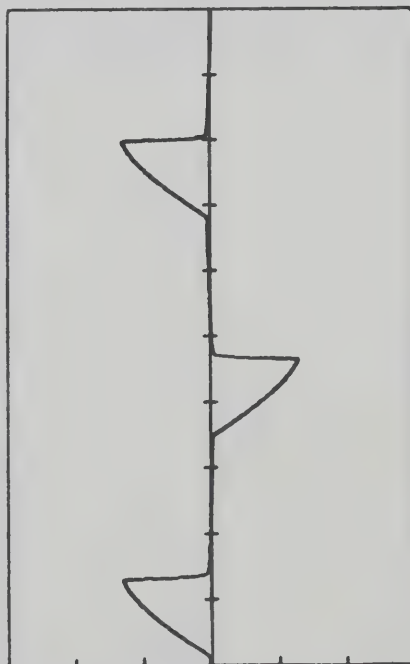
FIG. 3.9
Experimental and computed voltage waveforms for $E_C = 15$



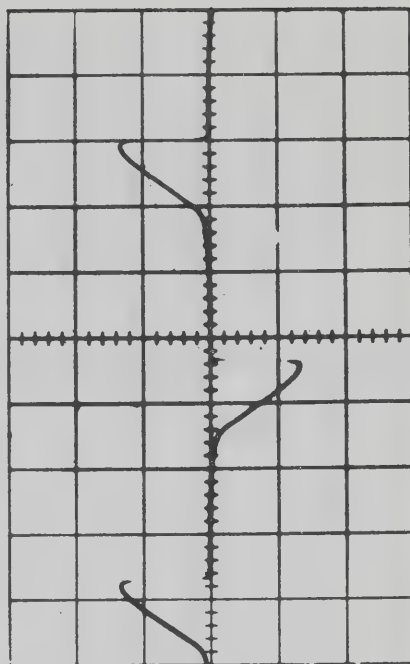
(a)



(c)



(b)



(d)

FIG. 3.10
Experimental and computed voltage waveforms for $E_C = 20$

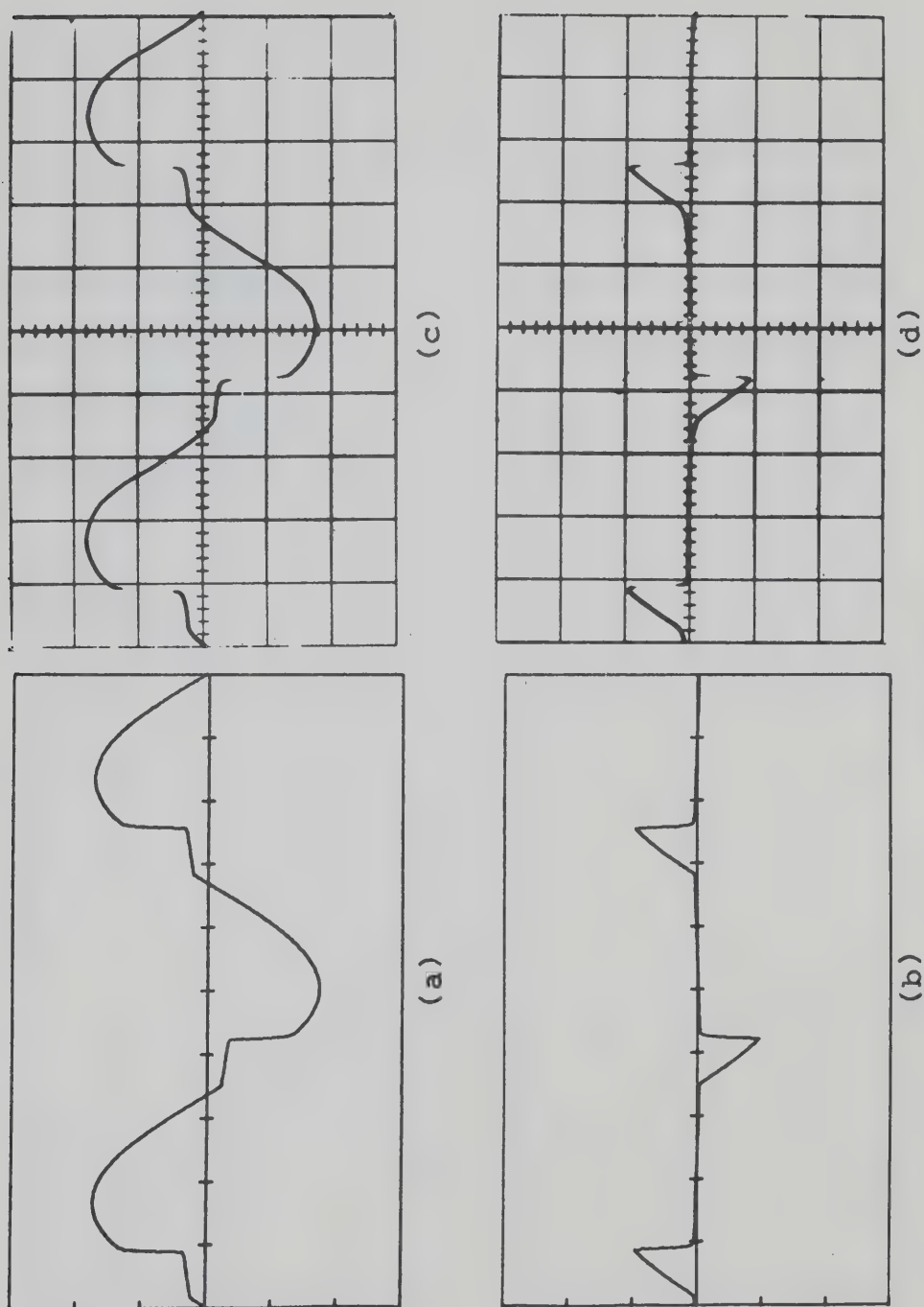
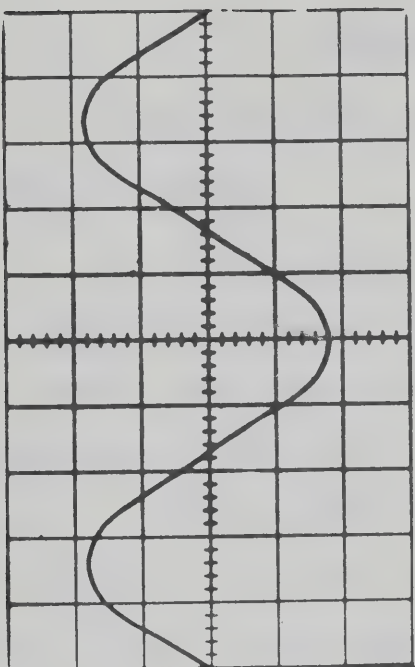
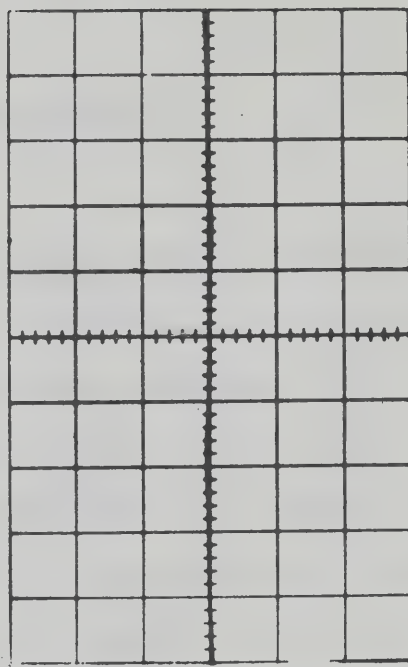


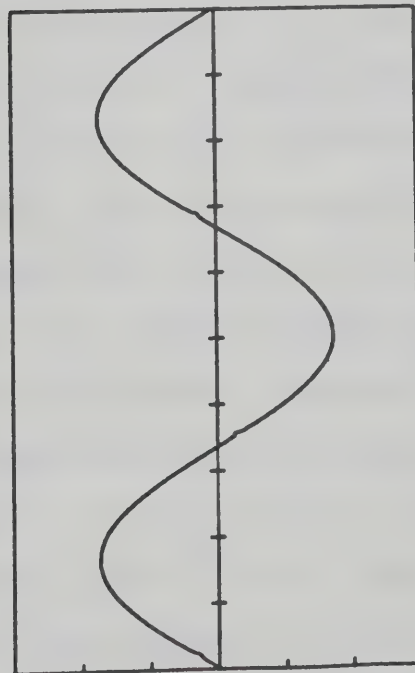
FIG. 3.11
Experimental and computed voltage waveforms for $E_C = 25$



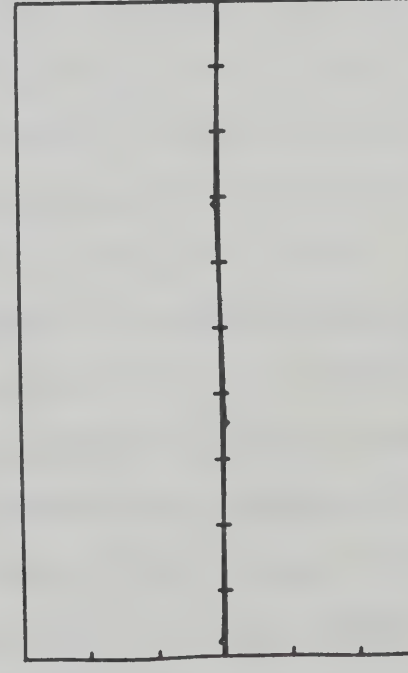
(a)



(b)



(c)



(d)

FIG. 3.12

Experimental and computed voltage waveforms for $E_C = 30$

CHAPTER 4

SERIES-CONNECTED MAGNETIC AMPLIFIER

4.1 Theory of operation

The circuit diagram of a series-connected non-feedback magnetic amplifier is shown in Fig. 4.1 [10-11-13]. The same two saturable reactors used for the parallel case is employed. The two gate windings are connected in series with their polarities such that any a.c. voltage applied across them induces no current in the control circuit. On the load side of the series-connected magnetic amplifier the a.c. voltage source e_s is in series with the load and in series with the two gate windings, the magnetic amplifier output is the a.c. voltage across the load R_L . If d.c. output is required a bridge rectifier can be used. The control side is similar to that of the parallel-connected magnetic amplifier with the exception that the value of R_C is lower. For $E_C = 0$, no d.c. current flows in the control winding N_C and each of the gate windings will have large inductive impedance. Thus most of the a.c. voltage e_s is across the gate windings and a negligible a.c. voltage appears across R_L . For $E_C \neq 0$, in one half cycle the flux linkage due to the d.c. control current i_C adds to the a.c. flux linkage of the first gate winding, and opposes that of the second gate winding. The high value of flux linkage of the first gate winding drives it

towards saturation and the impedance across this first gate becomes very small, practically a short circuit. At the same time there is a low value of flux in the second gate winding causing it to have a high input impedance. Due to the transformer action this high impedance is in parallel with the low value of resistance $R_C \left(\frac{N_g}{N_C} \right)^2$ resulting in a low impedance across the terminals of the second gate winding. Therefore, during this half cycle the impedance across the series connection of the two gate windings remains small and most of the a.c. voltage appears across the load. During the next half cycle the same action takes place but the two gate windings replace each other in action and still most of the a.c. voltage appears across the load. Thus in the presence of E_C most of the a.c. voltage appears across R_L . The amplitude of the load voltage together with its waveform are completely dependent on the magnitude of E_C .

4.2 Analysis

As in the case of the parallel-connected magnetic amplifier, the first step in the analysis is to replace each of the two iron-core transformers, Fig. 4.1, with the equivalent nonlinear lumped circuit model, Fig. 2.4. The characteristics of the nonlinear resistors and inductors are the same as for the parallel case since these do not depend on the external connection of the transformers. Thus, the series-connected magnetic amplifier is completely represented

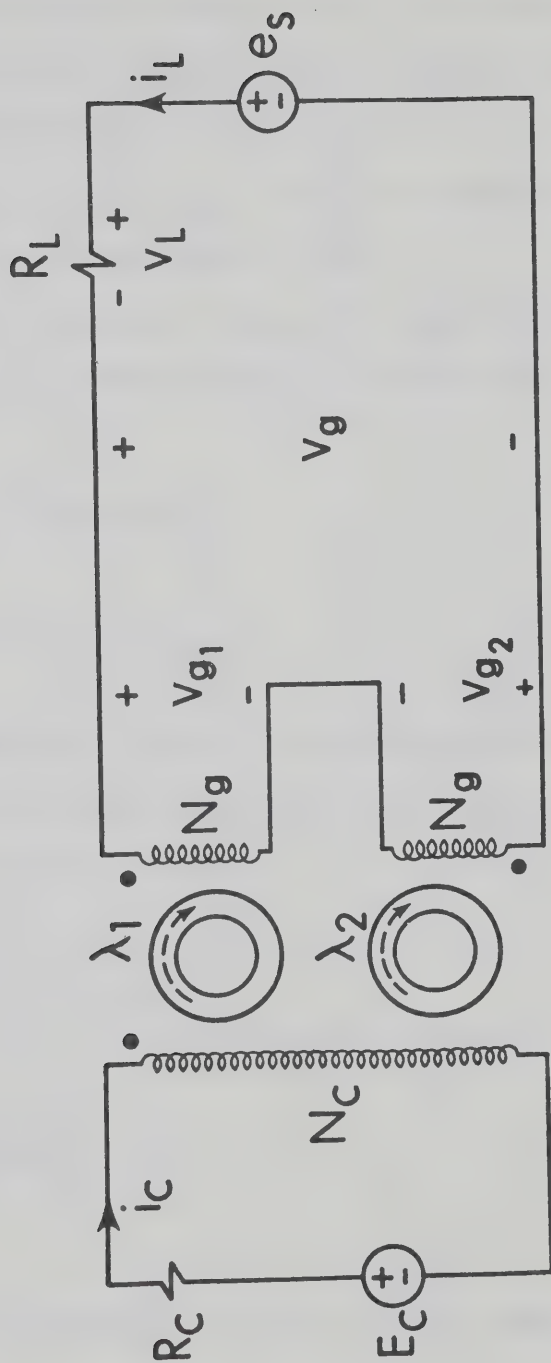


FIG. 4.1

Series-connected magnetic amplifier

by the equivalent circuit shown in Fig. 4.2. Replacing the ideal transformers with the controlled source representation, the equivalent circuit takes the form shown in Fig. 4.3. $v_1, v_2, e_s, R_L, R_C, E_C, i_{L_1}, i_{L_2}, i_{R_1}, i_{R_2}$, and $\frac{N_C}{N_g}$ are still the same as explained before in the parallel case.

With reference to Fig. 4.3, applying Kirchhoff current law to nodes 1 and 2 the currents in the nonlinear inductances are,

$$i_{L_1} = i_L + 20 i_C - i_{R_1} \quad (4.1)$$

$$i_{L_2} = -i_L + 20 i_C - i_{R_2} \quad (4.2)$$

With reference to Fig. 4.3, applying Kirchhoff voltage law and rearranging the resulting equations, the control current i_C and the load current i_L are

$$i_C = \frac{E_C - 20 (v_1 + v_2)}{R_C} \quad (4.3)$$

$$i_L = \frac{e_s - (v_1 - v_2)}{R_L + R_{g_1} + R_{g_2}} \quad (4.4)$$

Substitution in equations (4.1) and (4.2) by equations (3.7), (4.3) and (4.4) the currents i_{L_1} and i_{L_2} are

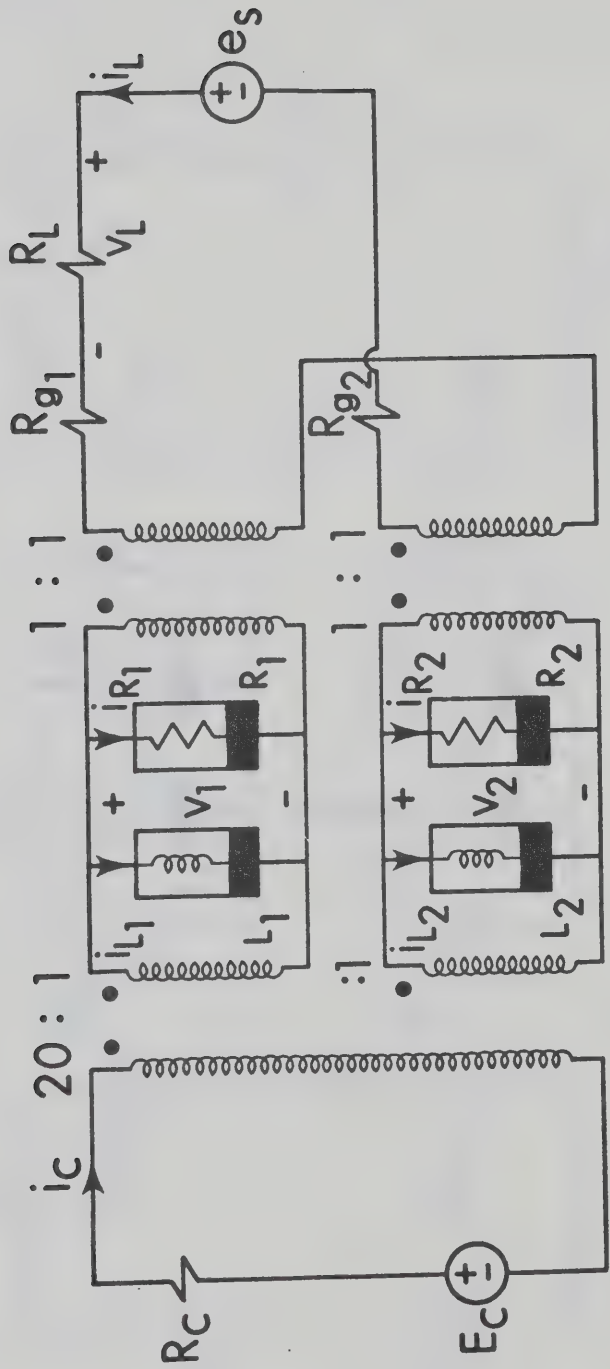


FIG. 4.2

The equivalent circuit for the series-connected magnetic amplifier using the nonlinear lumped circuit model

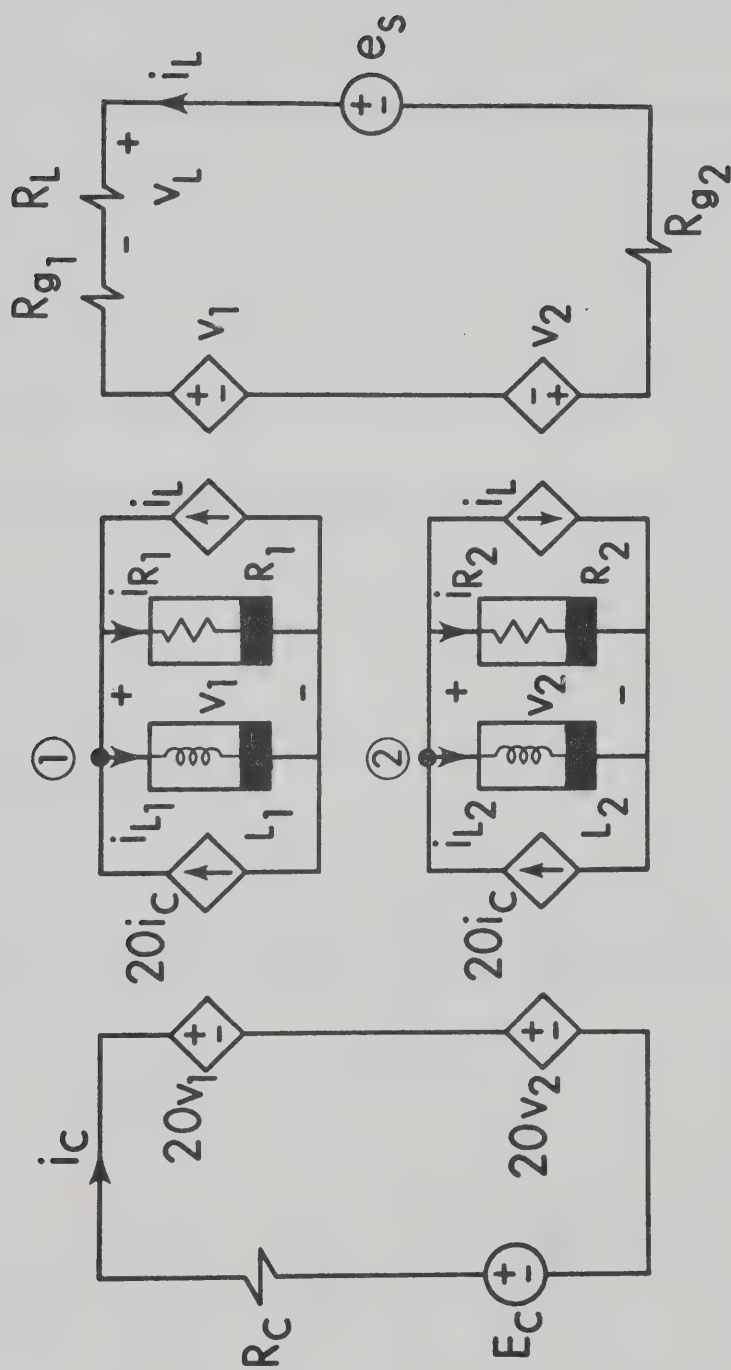


FIG. 4.3

Circuit diagram for the series-connected magnetic amplifier replacing ideal transformers by equivalent controlled source representation

$$i_{L_1} = \frac{e_s - v_1 + v_2}{R} + 20 \frac{E_C - 20 (v_1 + v_2)}{R_C} - h(v_1) \quad (4.5)$$

$$i_{L_2} = \frac{-e_s + v_1 - v_2}{R} + 20 \frac{E_C - 20 (v_1 + v_2)}{R_C} - h(v_2) \quad (4.6)$$

Where

$$R = R_L + R_{g_1} + R_{g_2} \quad (4.7)$$

But from the characteristics of L_1 and L_2 , the currents i_{L_1} and i_{L_2} are

$$i_{L_1} = f(\lambda_1)$$

$$i_{L_2} = f(\lambda_2)$$

Thus

$$f(\lambda_1) = \frac{E_s \sin \omega t}{R} + 20 \frac{E_C}{R_C} + v_2 \left(\frac{1}{R} - \frac{400}{R_C} \right) - v_1 \left(\frac{1}{R} + \frac{400}{R_C} \right) - h(v_1) \quad (4.8)$$

$$f(\lambda_2) = \frac{-E_s \sin \omega t}{R} + 20 \frac{E_C}{R_C} + v_1 \left(\frac{1}{R} - \frac{400}{R_C} \right) - v_2 \left(\frac{1}{R} + \frac{400}{R_C} \right) - h(v_2) \quad (4.9)$$

Equations (4.8) and (4.9) are two nonlinear coupled differential equations in λ_1 and λ_2 . As stated before no analytical solution is available and in order to solve these two equations numerically they should be put in the normal form. As in the parallel case this is impossible without using the piecewise linearization technique to relate the nonlinear resistors currents i_{R_1} and i_{R_2} to the voltages v_1 and v_2 respectively. As a result of this piecewise linearization technique the two currents i_{R_1} and i_{R_2} are put in the form previously given

$$i_{R_1} = h(v_1) = \sum_{K=1}^7 G_{K1} v_1 + \sum_{K=1}^7 I_{K1} \quad K=1,2,\dots, 7$$

$$i_{R_2} = h(v_2) = \sum_{m=1}^7 G_{m2} v_2 + \sum_{m=1}^7 I_{m2} \quad m=1,2,\dots, 7$$

As before the values of K and m are dependent on the values of v_1 and v_2 respectively. Substitution in equation (4.8) and (4.9) for $h(v_1)$, $h(v_2)$ and collecting terms of v_1 together and those of v_2 together the two equations can be put in the form,

$$\begin{bmatrix} f(\lambda_1) - \frac{E_s \sin \omega t}{R} - \frac{20E_C}{R_C} + \sum_{K=1}^7 I_{K1} \\ f(\lambda_2) + \frac{E_s \sin \omega t}{R} - \frac{20E_C}{R_C} + \sum_{m=1}^7 I_{m2} \end{bmatrix} = \begin{bmatrix} T_s \end{bmatrix} \begin{bmatrix} v_1 \\ v_2 \end{bmatrix} \quad (4.10)$$

Where

$$\begin{bmatrix} T_s \end{bmatrix} = \begin{bmatrix} -\frac{1}{R} - \frac{400}{R_C} - K^G_1 & \frac{1}{R} - \frac{400}{R_C} \\ \frac{1}{R} - \frac{400}{R_C} & -\frac{1}{R} - \frac{400}{R_C} - m^G_2 \end{bmatrix} \quad (4.11)$$

Taking the inverse of this transformation matrix, v_1 and v_2 are given as

$$v_1 = \frac{d\lambda_1}{dt} = \frac{1}{|T_s|} \left\{ \frac{E_s \sin \omega t}{R} \left[\frac{800}{R_C} + m^G_2 \right] - f(\lambda_1) \left[\frac{1}{R} + \frac{400}{R_C} + m^G_2 \right] + f(\lambda_2) \left[\frac{400}{R_C} - \frac{1}{R} \right] - K^I_1 \left[\frac{1}{R} + \frac{400}{R_C} + m^G_2 \right] + m^I_2 \left[\frac{400}{R_C} - \frac{1}{R} \right] + \frac{20E_C}{R_C} \left[m^G_2 + \frac{2}{R} \right] \right\} \quad (4.12)$$

$$v_2 = \frac{d\lambda_2}{dt} = \frac{1}{|T_s|} \left\{ \frac{-E_s \sin \omega t}{R} \left[\frac{800}{R_C} + K^G_1 \right] - f(\lambda_2) \left[\frac{1}{R} + \frac{400}{R_C} + K^G_1 \right] + f(\lambda_1) \left[\frac{400}{R_C} - \frac{1}{R} \right] - m^I_2 \left[\frac{1}{R} + \frac{400}{R_C} + K^G_1 \right] + K^I_1 \left[\frac{400}{R_C} - \frac{1}{R} \right] + \frac{20E_C}{R_C} \left[K^G_1 + \frac{2}{R} \right] \right\} \quad (4.13)$$

Where

$$|T_s| = \text{determinant of the matrix } [T_s].$$

These two differential equations are in the normal form relating the fluxes λ_1 and λ_2 with time t . The values of K and m are dependent on the values of v_1 and v_2 respectively. The determinant $|T_s|$ has a finite non-zero value for all possible combinations of K and m . Similar to the parallel case it is found that the two right hand sides of equations (4.12) and (4.13) satisfy the two conditions of the Cauchy-Lipschitz theorem, thus these two equations have a unique solution for all values of $t \geq 0$. This solution provides λ_1 , λ_2 , v_1 and v_2 as function of time t . But v_1 and v_2 cannot be measured and the measurable quantities in case of the series-connected magnetic amplifier are the voltages across the two gate windings v_{g1} , v_{g2} , v_g and the load voltage v_L . These are related to the voltages v_1 , v_2 and e_s as

$$v_{g1} = E_s \frac{R_{g1}}{R} \sin \omega t + v_1 \left[1 - \frac{R_{g1}}{R} \right] + v_2 \frac{R_{g1}}{R} \quad (4.14)$$

$$v_{g2} = -E_s \frac{R_{g2}}{R} \sin \omega t + v_2 \left[1 - \frac{R_{g2}}{R} \right] + v_1 \frac{R_{g2}}{R} \quad (4.15)$$

$$v_g = v_{g1} - v_{g2} \quad (4.16)$$

$$v_L = E_s \sin \omega t - v_g \quad (4.17)$$

4.3 Numerical Computation

To start the numerical computation, it is necessary to calculate the initial values of λ_1 and λ_2 at $t = 0$, namely, $\lambda_1(0)$ and $\lambda_2(0)$. Following the same reasoning as in the case of parallel-connected magnetic amplifier it is found that,

$$v_1(0) = v_2(0) = 0 \quad (4.18)$$

$$\lambda_1(0) = \lambda_2(0) = f^{-1} \left(20 \frac{E_C}{R_C} \right) \quad (4.19)$$

These initial conditions clearly satisfy the equation (4.10).

The same computer program used in the case of the parallel-connected magnetic amplifier is used here with the exception that the subroutines FCT and OUTP are changed. The new FCT subroutine is written to compute the values of $\frac{d\lambda_1}{dt}$ and $\frac{d\lambda_2}{dt}$ for any given λ_1 , λ_2 and t using equations (4.12) and (4.13). The new OUTP subroutine calculates and stores values of the load voltage v_L , the gate voltages v_{g_1} , v_{g_2} and v_g , then plots v_L , v_g and v_{g_1} versus time t .

The steady state waveforms of v_L , v_{g_1} and v_g were plotted versus time for values of E_C equal to 0.0, 10, 20, 30 and 40 volts. These waveforms are shown in Figs. 4.4(a), (b) and (c) to Figs. 4.8(a), (b) and (c). The a.c. voltage source e_s has an amplitude equal to 25 volts and frequency of 60 Hz. The values of the resistors used in the

calculation are exactly equal to those used in the practical circuit of the series-connected magnetic amplifier.

4.4 Experimental results

The values of the parameters of the circuit used in experimental investigation are the same as those used in the parallel-connected magnetic amplifier experimental investigation except that the value of R_C now is $5\text{ K}\Omega$ and amplitude of e_s is 25 volts.

The values of the d.c. control voltage are taken as 0.0, 10, 20, 30 and 40 volts. For each of these values the steady state waveforms of v_L , v_g and v_{g_1} were photographed. These waveforms are shown in Figs. 4.4(d), (e) and (f) to Figs. 4.8(d), (e) and (f). In each of these photos the time scale was 2.5 ms /division and the voltage scale was 10 volts/division .

4.5 Comparison

The accuracy of the mathematical model in predicting the accurate performance of the series-connected magnetic amplifier is checked by comparing the waveforms computed and plotted from the analysis with the actual experimental waveforms. The waveforms of three voltages are compared, namely, the load voltage v_L , the voltage across the terminals of the first gate winding v_{g_1} and the voltage across the two gate windings v_g . The comparison was carried out for values of the d.c. control voltage E_C equal to 0.0, 10, 20, 30 and 40 volts.

The waveforms corresponding to these values are shown in Figs. 4.4 to 4.8. Figures (a), (b) and (c) show the waveforms of v_L , v_g and v_{g_1} respectively, computed using the mathematical model. Figures (d), (e) and (f) show the actual experimental waveforms of v_L , v_g and v_{g_1} . It is clear that the amplitude of v_{g_1} is nearly half that of v_g . It is also clear that for either the experimental waveforms or those plotted from the modeling analysis, the sum of v_g and v_L is always equal to the sinusoidal voltage $E_s \sin(2\pi 60)t$.

Fig. 4.4 was obtained for $E_C = 0.0$ volts. The load voltage is of a very small amplitude while the gate voltages are nearly sinusoidal. The agreement concerning both amplitudes and waveforms is excellent except for the sudden sharp changes in the waveforms in Figs. 4.4(a), (b) and (c).

As the magnitude of the d.c. control voltage E_C increases, the load resistor R_L starts to have most of the a.c. voltage across its terminals and the duration over which this occurs increases as E_C increases, Figs. 4.4 to 4.8, till the load voltage v_L becomes nearly sinusoidal at $E_C = 40$ volts, Fig. 4.8. Figures 4.4 to 4.8 show excellent agreement between the waveforms of v_L , v_g and v_{g_1} in Figs. (a), (b) and (c) and those in Figs. (d), (e) and (f) respectively. The agreement is excellent concerning the amplitudes of these voltages as well as their waveforms.

Thus except for this slight difference, in the form of sudden sharp change of the voltage in those waveforms computed using the model, the mathematical model successfully predicts the accurate performance.

of the series-connected non-feedback magnetic amplifier. As stated in the parallel case this may be the results of using the piecewise linearization technique in interpolating the characteristics of the nonlinear elements together with some inaccuracy of the model.

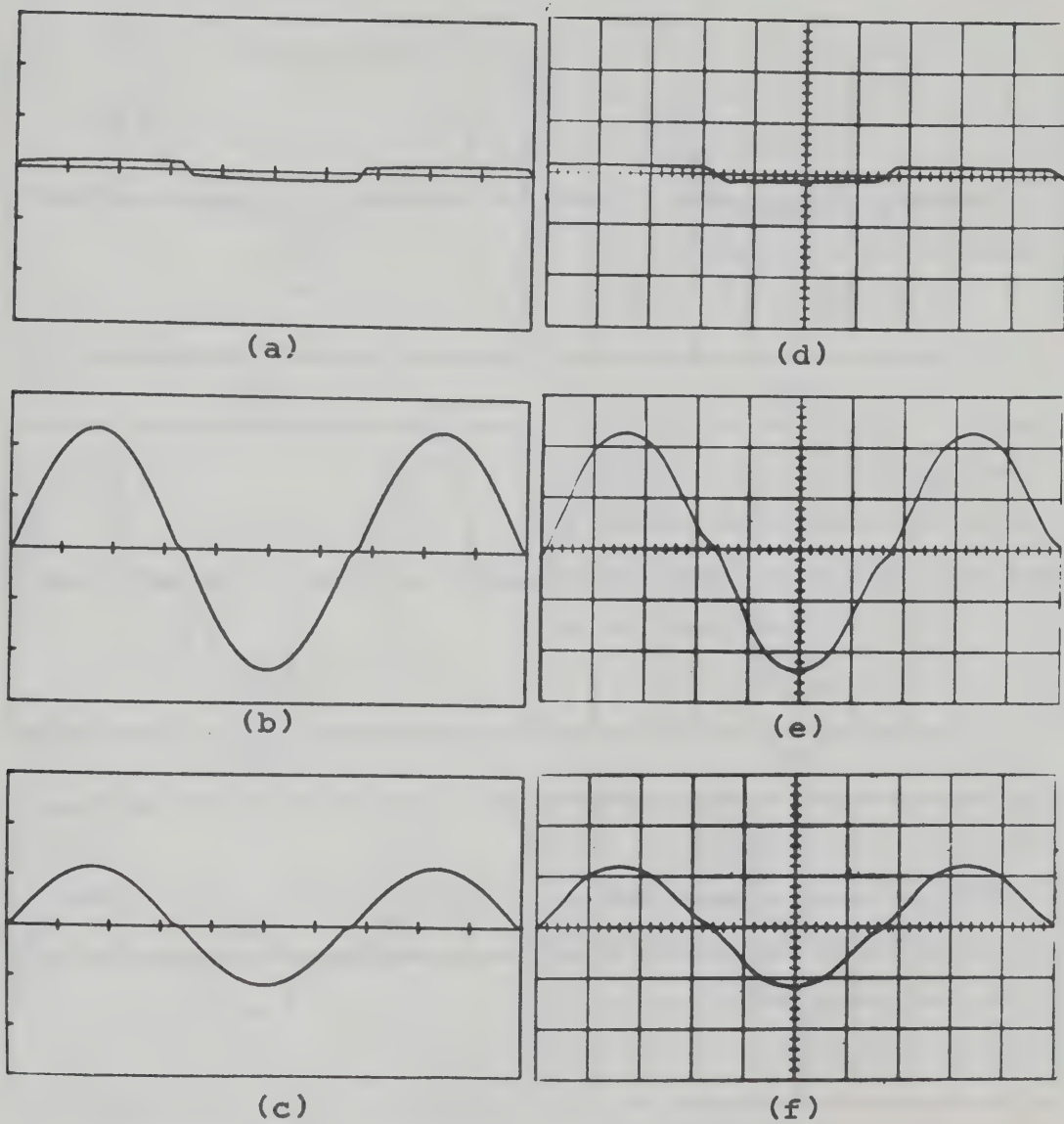


FIG. 4.4

Experimental and computed voltage waveforms for $E_C = 0.0$

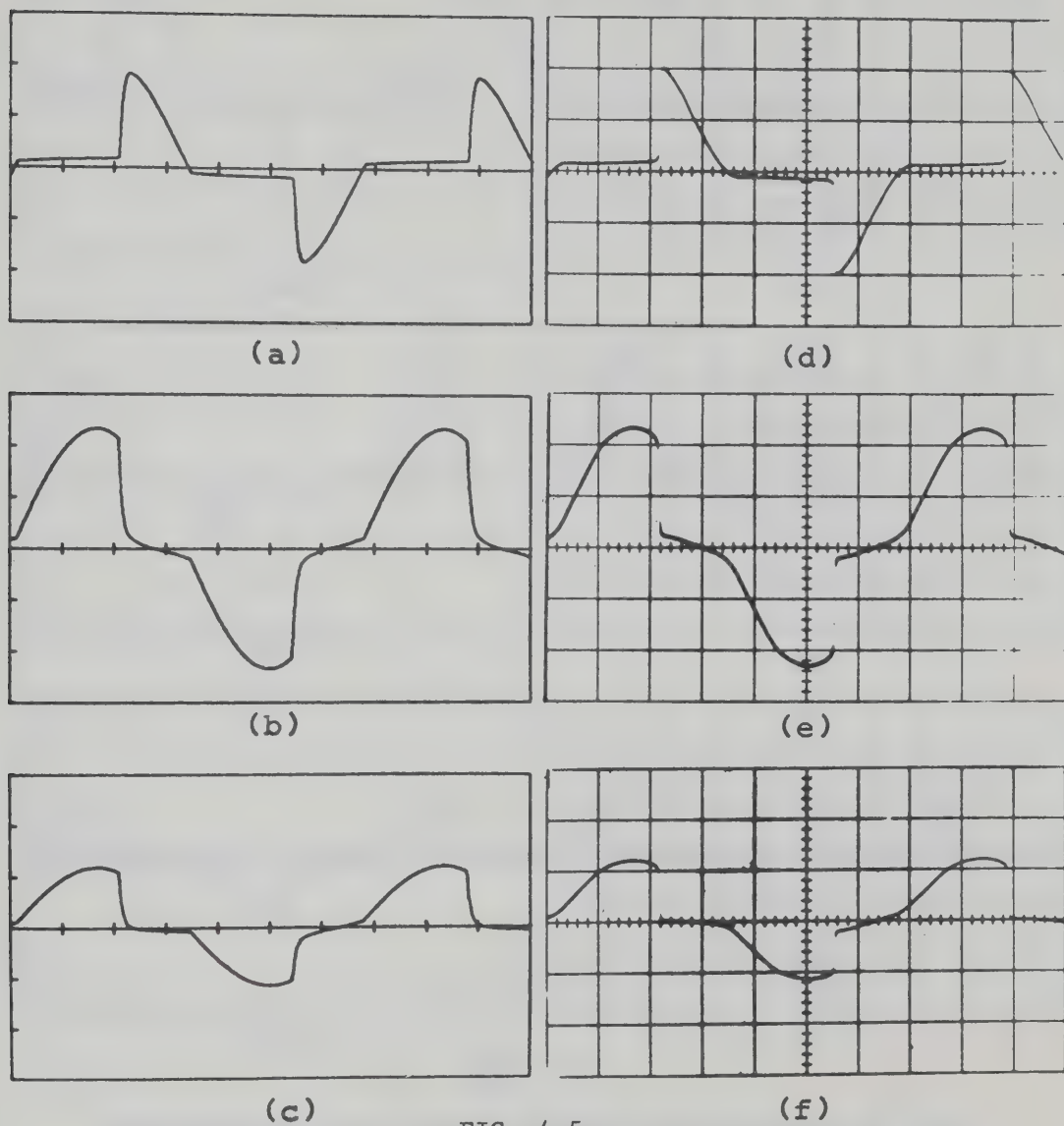


FIG. 4.5

Experimental and computed voltage waveforms for $E_C = 10$

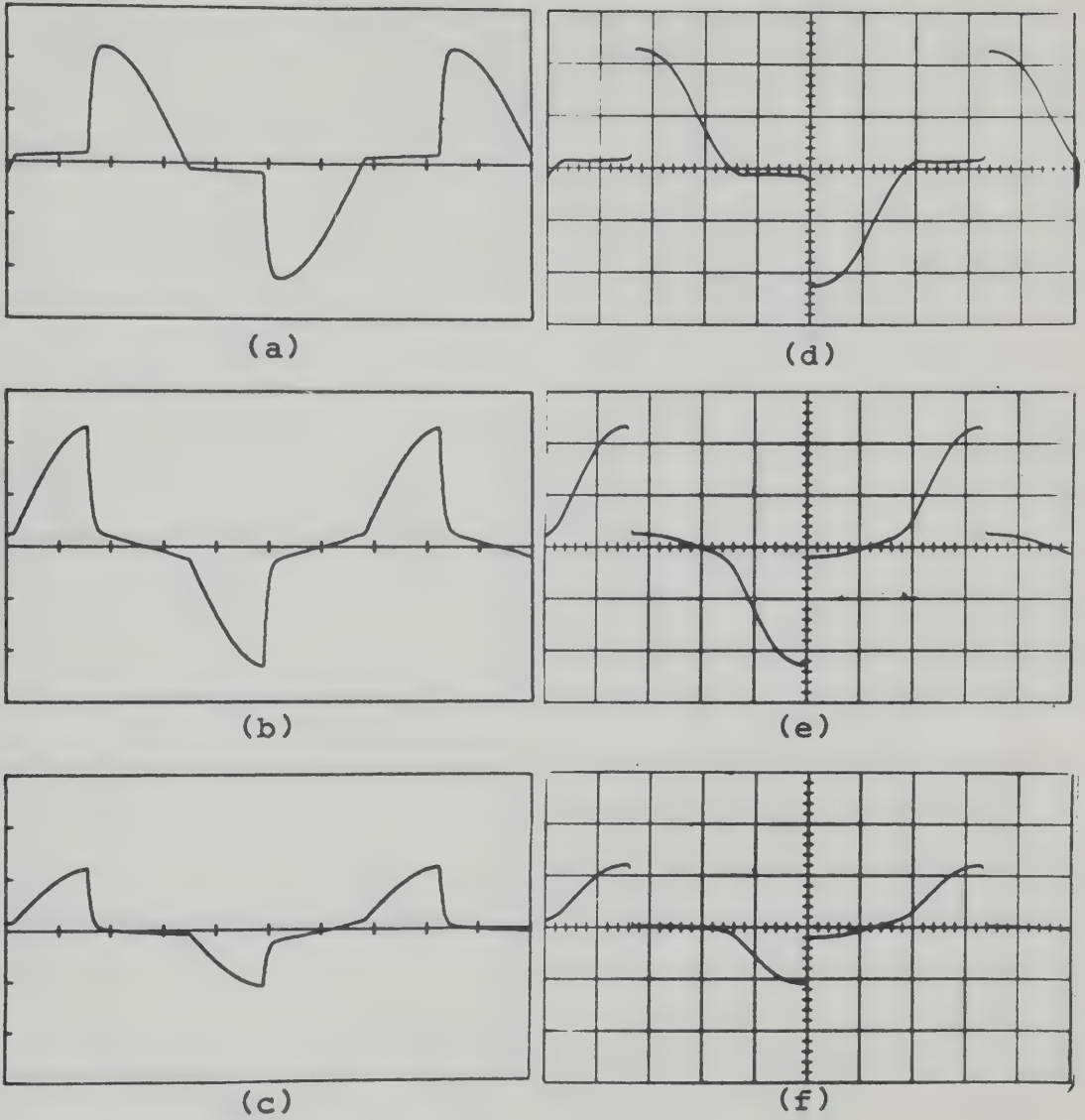
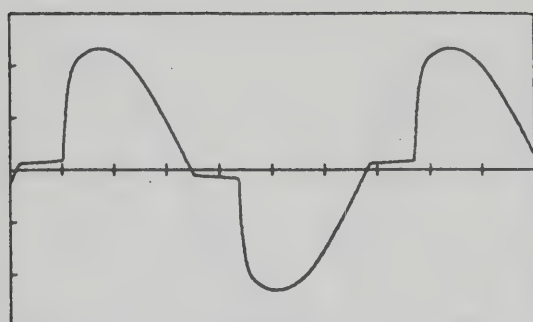
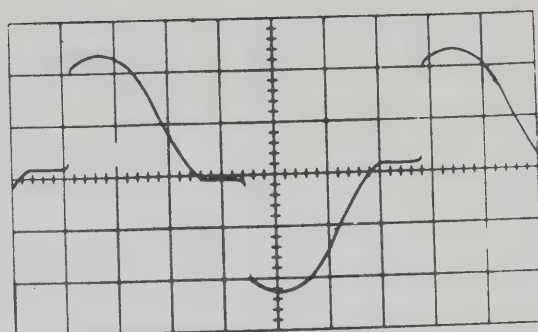


FIG. 4.6

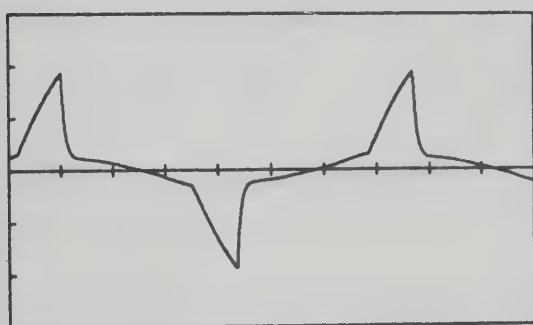
Experimental and computed voltage waveforms for $E_C = 20$



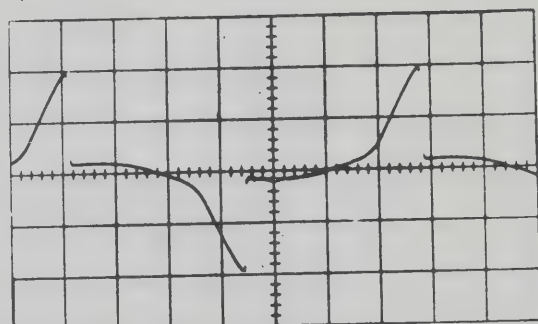
(a)



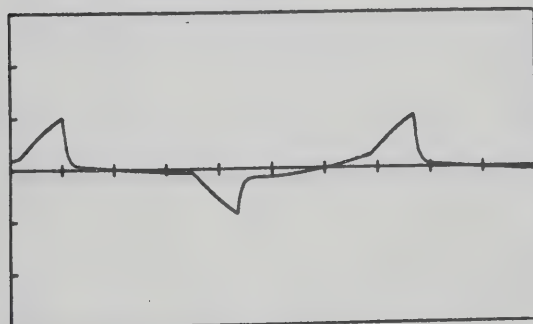
(d)



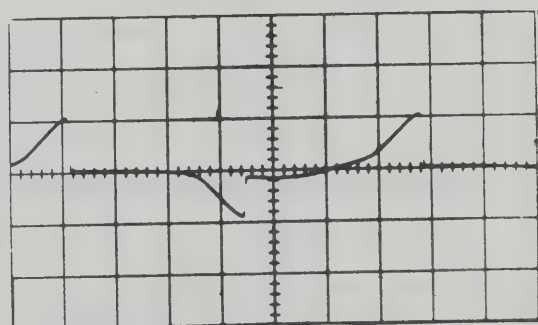
(b)



(e)



(c)



(f)

FIG. 4.7

Experimental and computed voltage waveforms for $E_C = 30$

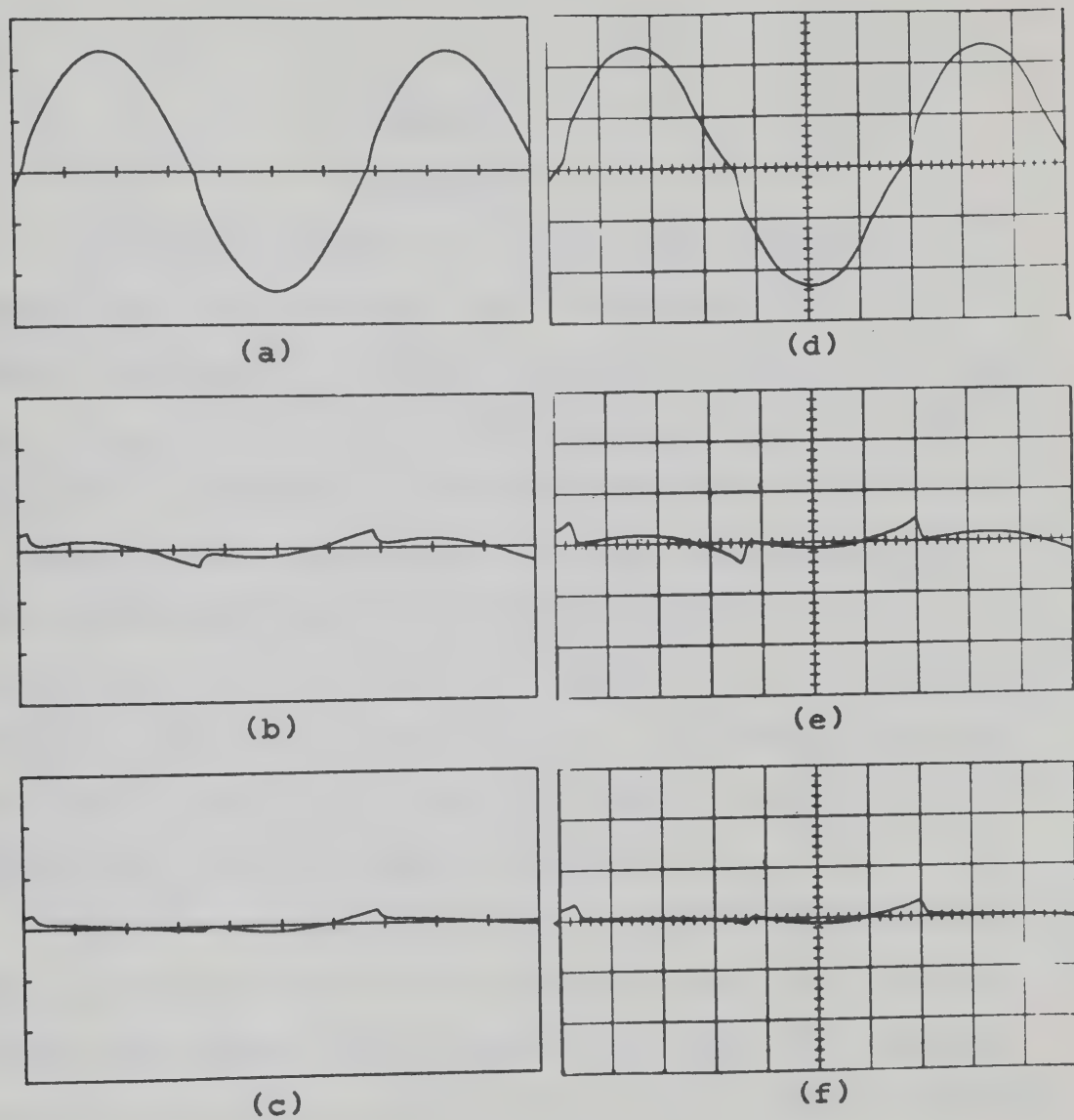


FIG. 4.8

Experimental and computed voltage waveforms for $E_C = 40$

CHAPTER 5

CONCLUSION

The mathematical model used in this work to represent the magnetic iron-cores was proved once to successfully predict the correct performance of a push-pull tunnel-diode relaxation oscillator with a single iron-core. This model was found to be a very simple and useful one especially in representing magnetic iron-cores since it yields a lumped circuit model. Since this is a postulated non-linear mathematical model, it is necessary to prove that it can predict the accurate performance of a large number of systems comprising hysteretic elements. In the present work it is found that the model successfully predicts the accurate performance of both the parallel and the series connected magnetic amplifiers.

First the parameters of the lumped circuit model were obtained from the hysteresis loop of the magnetic iron-core. Then the lumped circuit model replaces the two magnetic iron-cores. The resulting circuits for the parallel and the series connected magnetic amplifiers were analyzed and in both cases the resulting two differential equations were solved numerically.

The actual experimental waveforms were then compared to those computed from the analysis and it was found that for both types of connections the model is very successful in predicting the experimental

waveforms except for a very slight difference in the form of sharp points in the computed waveforms, which may be due to the use of the piecewise-linearization techniques in interpolating the characteristics of the nonlinear elements of the model together with any slight inexactness that the model may have. This slight inaccuracy may be avoided by adding some parasitic element to the model.

The only drawback in the simulation process of the parallel-connected and the series-connected magnetic amplifier circuits is the cost of the numerical computations. In case of the parallel-connected magnetic amplifier, steady state is reached after about 45 minutes of computation on the IBM 360 digital computer. In case of the series-connected magnetic amplifier the required time, of course smaller than in the parallel-connected case, is about 5 minutes. The time of computation may be reduced by finding more suitable initial conditions and using a numerical technique faster than the HPCG.

REFERENCES

- [1] I.W. McKeehan, Magnets. Princeton, N.J. :Van Nostrand 1967.
- [2] S. Chikazumi, Physics of Magnetism. New York :Wiley 1964.
- [3] A.H. Morrish, The Physical Principles of Magnetism. New York :
Wiley, 1965.
- [4] W.P. Mason and R.F. Wick, "Ferroelectrics and the dielectric
amplifier," Proc. IRE, Vol. 52, PP. 1606-1620
November 1964.
- [5] T.C. Ruch and H.D. Patton, Physiology and Biophysics, 19th ed.
Philadelphia, Pa. saunders, ch. 39, PP. 733-759, 1965.
- [6] O.I. Butler and M.R. Sarna, "Relaxation methods applied to the
problem of ac magnetization of ferromagnetic laminae,"
Proc. IEE (London), pt. 2, PP. 389-398, 1951.
- [7] R.J.P. DeFigueiredo, "Forced oscillations in nonlinear systems
with hysteresis," IRE Trans. Circuit Theory, vol. CT-12,
PP. 52-58, March 1965.
- [8] L.O. Chua and K.A. Stromsmoe, "Synthesis of lumped circuit models
for nonlinear inductors exhibiting hysteresis loops,"
IEEE Trans. Circuit Theory, CT-19, November 1970.
- [9] L.A. Zadeh and C.A. Desoer, Linear System Theory, The State Space
Approach, New York : McGraw-Hill, 1963.

- [10] Sidney Platt, Magnetic Amplifier Theory and Application.
Englewood Cliffs, Prentice-Hall, 1958.
- [11] William A. Geyger, Magnetic Amplifier Circuits. McGraw-Hill,
1957.
- [12] F.F. Kuo and W.G. Magnuson, Jr., Computer-Oriented Circuit Design.
Englewood Cliffs, N.J. : Prentice-Hall, 1969.
- [13] H.F. Storm, Magnetic Amplifiers. New York : Wiley, 1955.
- [14] K. Ogata, State Space Analysis of Control Systems. Englewood
Cliffs, Prentice-Hall, 1967.
- [15] IBM, System/360 Scientific Subroutine Package.

APPENDIX A

THE PIECEWISE LINEARIZATION

TECHNIQUE

If only a finite number of points on the characteristics of a nonlinear element are known and it is required to calculate the coordinates of intermediate points, it is necessary to use some interpolating technique [12]. The piecewise linearization technique replaces the actual nonlinear curve, which join this point, with a number of linear segments. The break points of these segments are the known data points.

If the two variables are x and y and the number of given data points is S_j , then the nonlinear curve is replaced by (S_j-1) segments, where j is the nonlinear element number. Each of the segments is completely specified by:

- 1 - slope of the k^{th} segment = K_j^G
- 2 - Intersection of the k^{th} segment with the y axis = K_j^Y
- 3 - Interval of definition of the k^{th} segment, namely,
 $K_j^{Y^-} < y_j < K_j^{Y^+}$, $K_j^{X^-} < x_j < K_j^{X^+}$.

Fig. (A.1) shows a typical K^{th} segment illustrating various symbols defined above.

If the nonlinear element is a resistor the variables x and y are the voltage v_R and the current i_R . If the nonlinear element is an inductor the x and y are the current i_L and flux λ .

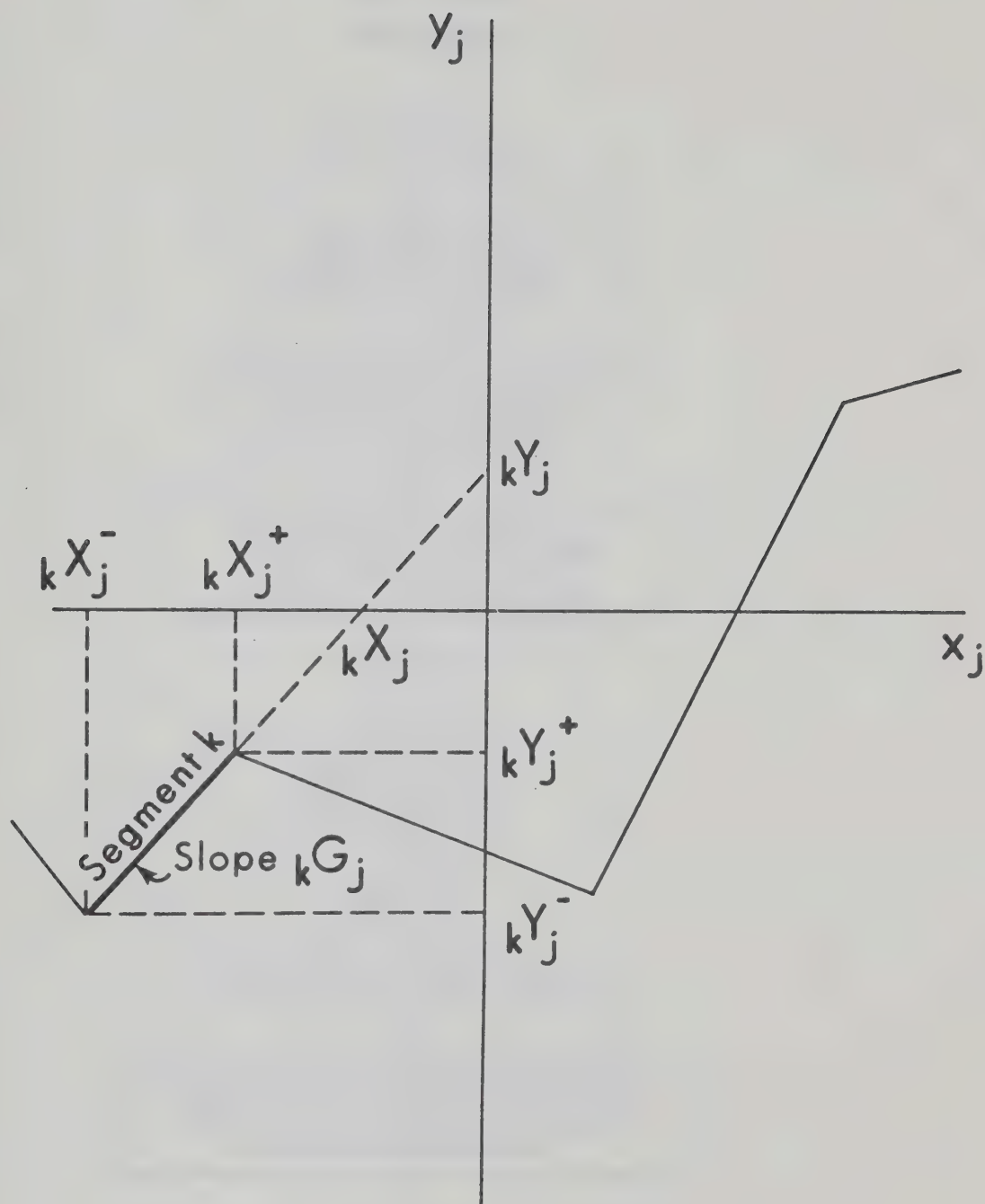
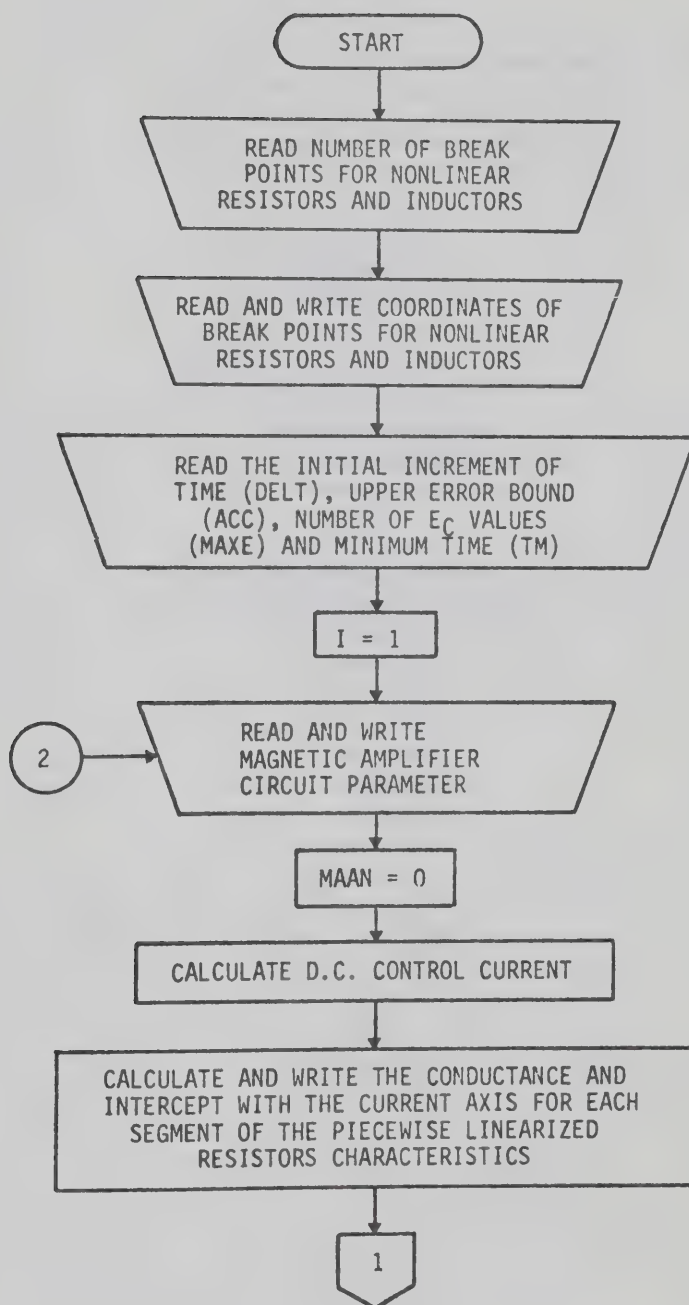
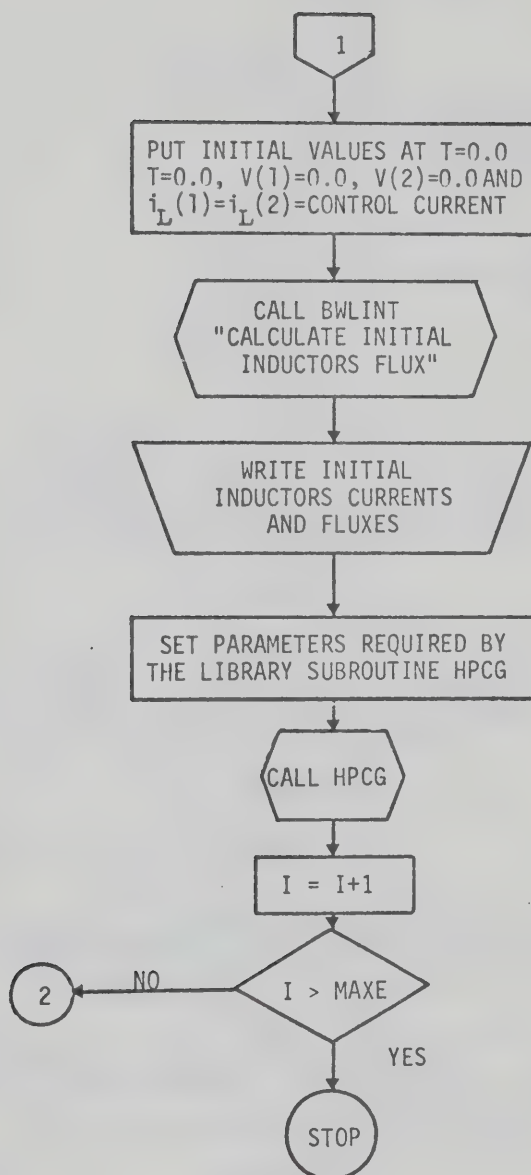


FIG. A.1

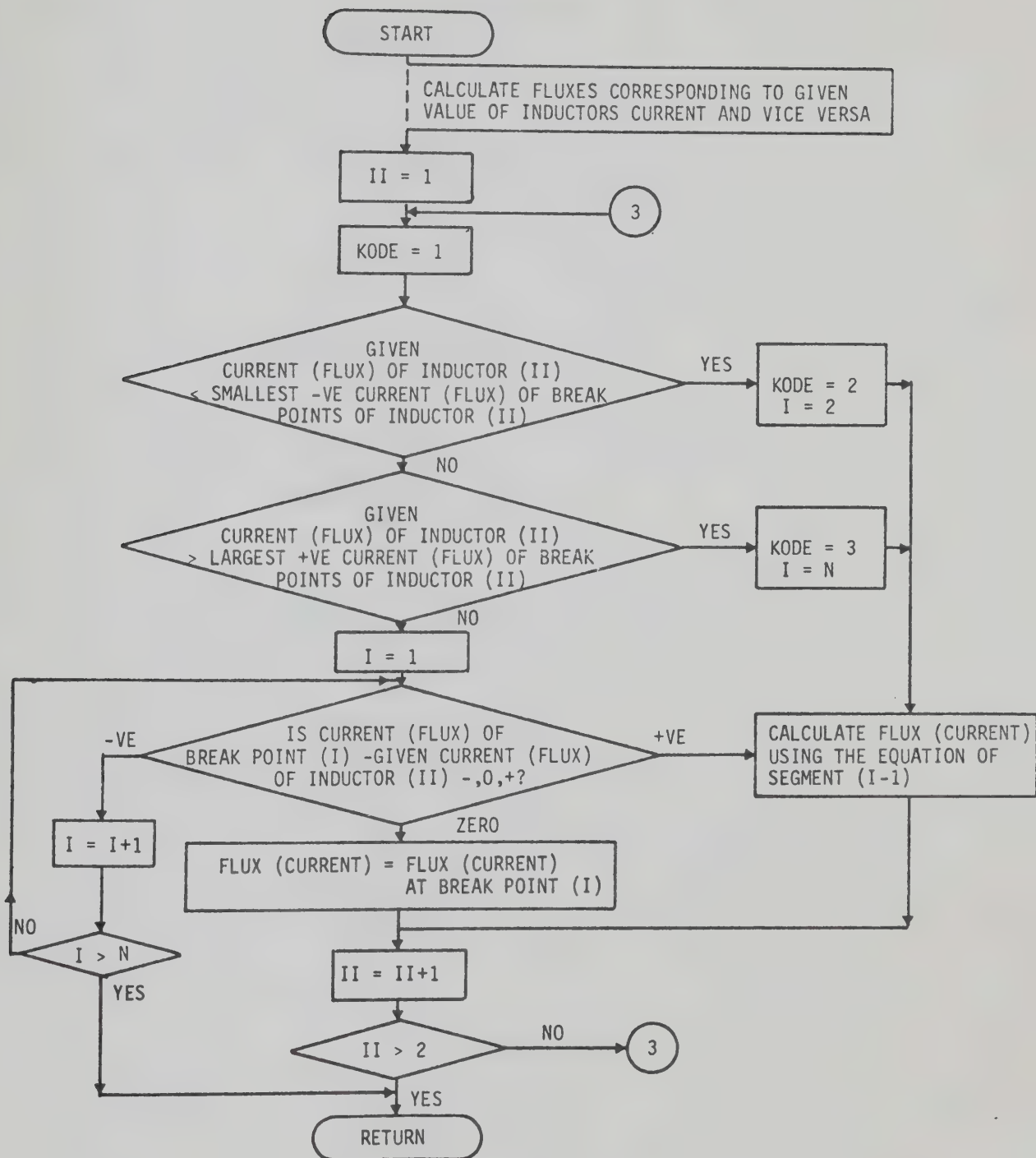
The parameters defining a piecewise-linear segment

APPENDIX B
FLOW CHARTS
MAIN PROGRAM

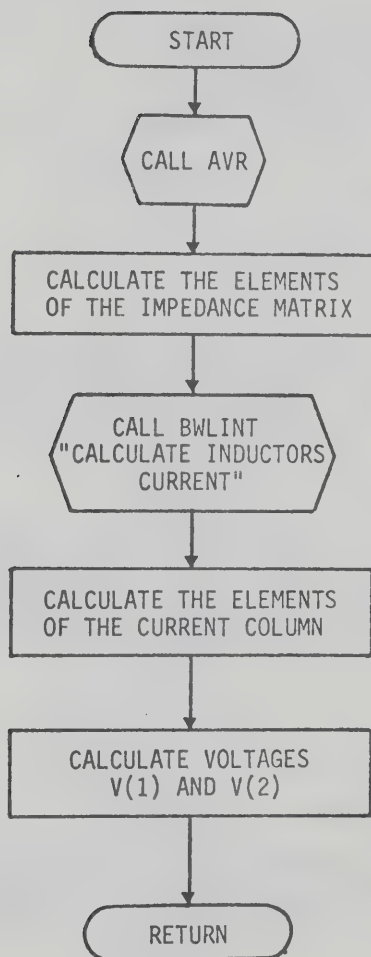




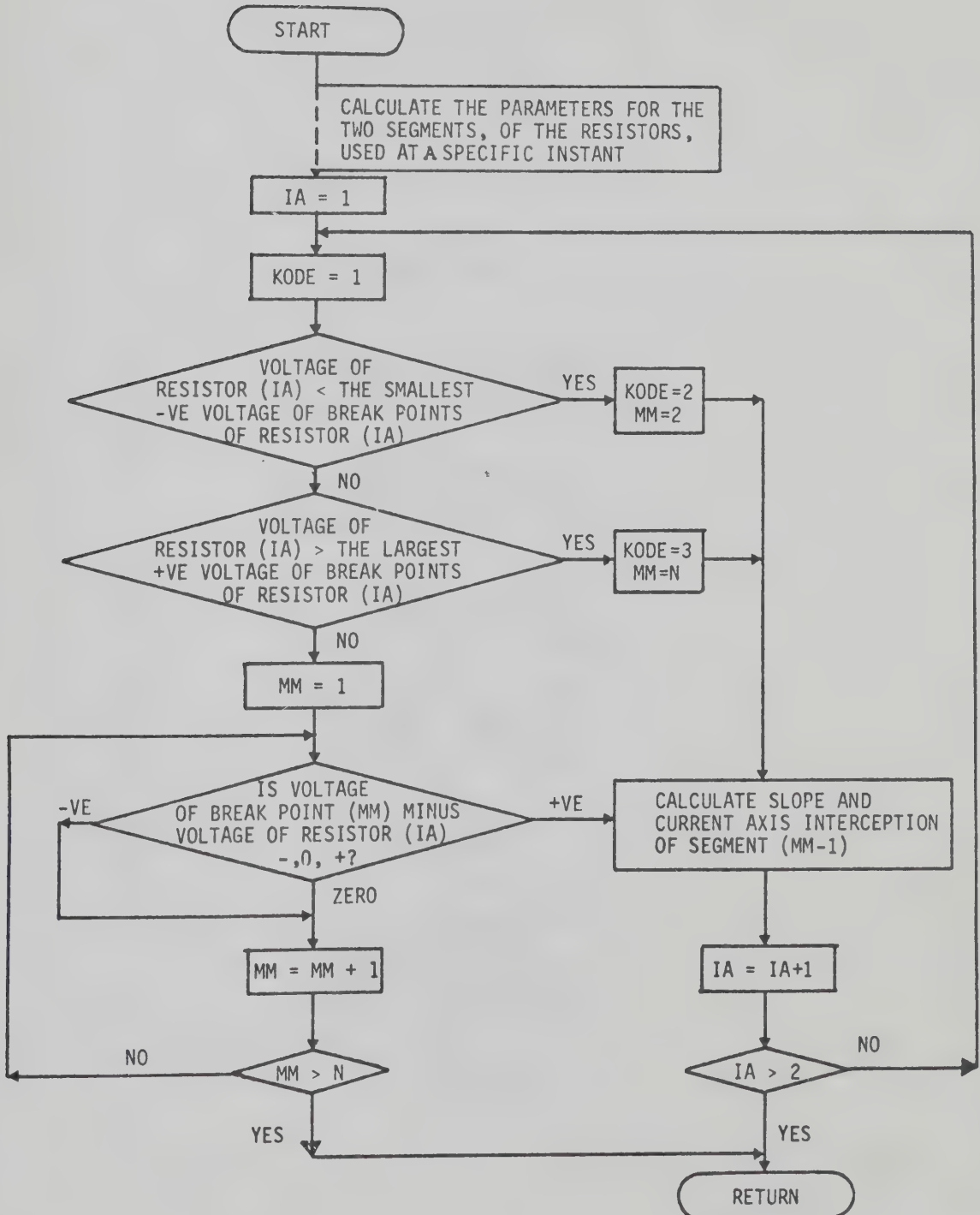
SUBROUTINE BWLINT



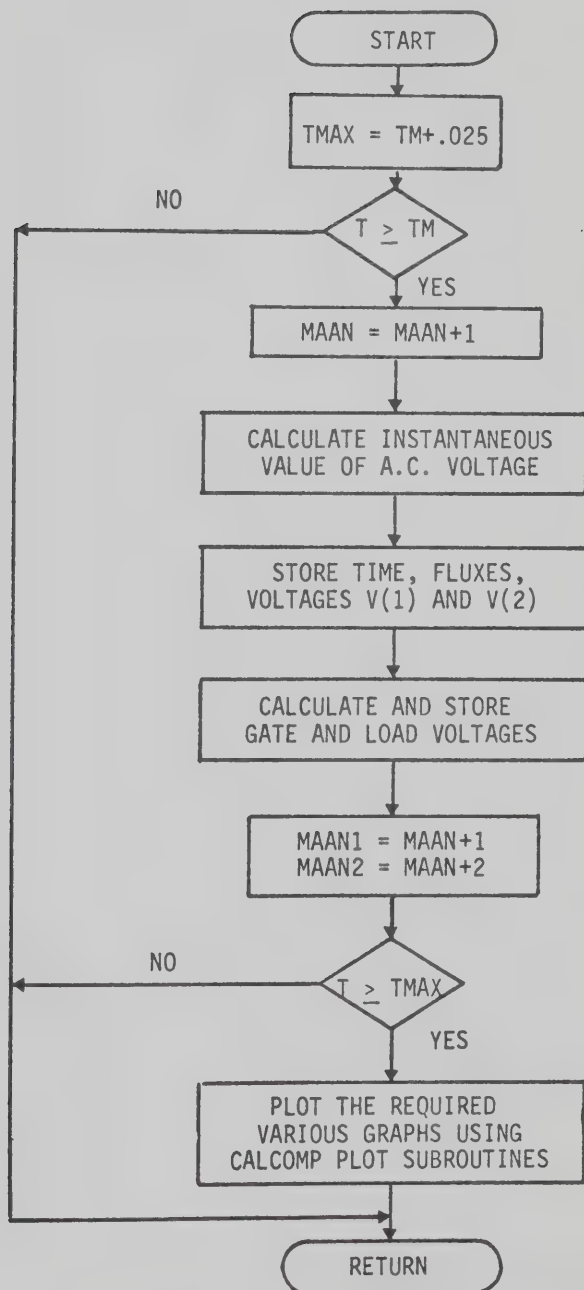
SUBROUTINE FCT



SUBROUTINE AVR



SUBROUTINE OUTP



B30002